Dynamic persistence of intracellular bacterial communities of uropathogenic *Escherichia coli* in a human bladder-chip model of urinary tract infections

Authors: Kunal Sharma, Neeraj Dhar*[&], Vivek V. Thacker*[&], Thomas M. Simonet, François Signorino-Gelo, Graham Knott, John D. McKinney*

Affiliations:

School of Life Sciences, Swiss Federal Institute of Technology in Lausanne (EPFL), 1015 Lausanne, Switzerland.

[&] These authors contributed equally

*Correspondence to: neeraj.dhar@epfl.ch, vivekvthacker@gmail.com , john.mckinney@epfl.ch

Abstract

Uropathogenic *Escherichia coli* (UPEC) proliferate within superficial bladder umbrella cells to form intracellular bacterial communities (IBCs) during early stages of urinary tract infections. However, the dynamic responses of IBCs to host stresses and antibiotic therapy are difficult to assess *in situ*. We develop a human bladder-chip model wherein umbrella cells and bladder microvascular endothelial cells are co-cultured under flow in urine and nutritive media respectively, and bladder filling and voiding mimicked mechanically by application and release of linear strain. Using time-lapse microscopy, we show that rapid recruitment of neutrophils from the vascular channel to sites of infection leads to swarm and neutrophil extracellular trap formation but does not prevent IBC formation. Subsequently, we tracked bacterial growth dynamics in individual IBCs through two cycles of antibiotic administration interspersed with recovery periods which revealed that the elimination of bacteria within IBCs by the antibiotic was delayed, and in some instances, did not occur at all. During the recovery period, rapid proliferation in a significant fraction of IBCs reseeded new foci of infection through bacterial shedding and host cell exfoliation. These insights reinforce a dynamic role for IBCs as harbours of bacterial persistence, with significant consequences for non-compliance with antibiotic regimens.

Keywords: bladder-chip, uropathogenic *Escherichia coli* (UPEC), intracellular bacterial communities (IBCs), bacterial persistence, antibiotic treatment, neutrophil swarms, neutrophil extracellular traps, shear stress, stretching, confocal live-cell imaging

Introduction

Urinary tract infections (UTIs), the second most-common cause for the prescription of antibiotics (Foxman, 2010) are characterized by the high frequency of recurrence, defined as a reappearance of infection within 12 months despite the apparently successful completion of antibiotic therapy. Recurrence occurs in about 25% of all UTIs (Foxman et al., 2000) and strongly impacts the cost of healthcare and reduces the quality of life, particularly since more than 60% of women are diagnosed with a UTI at least once in their lifetime (Klein and Hultgren, 2020). Uropathogenic *Escherichia coli* (UPEC), the causative agent for the majority of UTIs, exhibits a complex lifestyle in the bladder, with planktonic sub-populations within the urine co-existing with intracellular bacteria. UPEC invasion of the urinary bladder generates substantial changes to bladder morphology and a robust immune response. Much of our current understanding of early stages of UTI and the intracellular lifestyle is derived from studies in the mouse model (Anderson et al., 2003; Duraiswamy et al., 2018; Hannan et al., 2012; Hung et al., 2009; Justice et al., 2004; Schwartz et al., 2011; Yang et al., 2019). Examinations of mouse bladder explants via microscopy have revealed the formation of intracellular bacterial communities (IBCs) composed of thousands of bacteria within individual superficial bladder cells (Justice et al., 2004). IBCs also play a prominent role in clinical infection and have also been harvested from the urine of cystitis patients (Robino et al., 2013; Rosen et al., 2007). These structures are considered to have a linear progression from an early stage of colonization by single bacteria to an intermediate stage of biofilm-like communities culminating in the release of bacteria at the late stage. However, long-term imaging of infected animals or of explant-tissue is technically challenging and therefore it has been difficult to capture the dynamic changes that underlie the formation of these structures and their impact on infection and clearance by subsequent antibiotic treatment.

58 In addition, the bladder is an extremely complex organ; it has a stratified architecture with well-
59 differentiated cell types; a lumen filled with urine whose composition and chemical properties
60 can vary depending on the physiological state of the individual and is subjected to periodic and
61 large changes in organ volume and surface area (Korkmaz and Rogg, 2007). These features may
62 play important roles in infection, but they have been hitherto hard to capture outside of a whole
63 animal model, where they are present in their entirety and cannot be dissected in a modular
64 manner.
65 Organotypic models are well-suited to address these outstanding questions. A key strength of
66 advanced organotypic models such as organs-on-chip (Benam et al., 2016; Huh et al., 2010a;
67 Jang et al., 2013, 2019; Kim et al., 2016; Novak et al., 2020; Zhou et al., 2016) or organoids
68 (Cakir et al., 2019; Clevers, 2016; Rossi et al., 2018; Sato et al., 2009) is that they increasingly
69 recapitulate the complexity of host physiology. Organ-on-chip models have been developed for
70 several organs either in isolation or in combination (Novak et al., 2020; Ronaldson-Bouchard
71 and Vunjak-Novakovic, 2018). These systems are increasingly being used to model infectious
72 diseases including viral and bacterial infections of the respiratory tract (Nawroth et al., 2020; Si
73 et al., 2020; Thacker et al., 2020b, 2020a), gut (Jalili-Firoozinezhad et al., 2019; Kim et al.,
74 2016; Shah et al., 2016; Tovaglieri et al., 2019), kidney (Wang et al., 2019), and liver (Kang et
75 al., 2017). Recently, bladder organoids that mimic the stratified architecture of the urothelium
76 have been used to study infections (Horsley et al., 2018; Smith et al., 2006; Sharma et al., 2020).
77 However, the organoid model suffers from certain shortcomings inherent to the 3-D architecture
78 such as the lack of vasculature, the inability to manipulate the cells mechanically, and the
79 constrained volume of the lumen. In contrast, organ-on-chip models offer a complementary
80 approach that does not suffer from these limitations. However, to our knowledge, there have

been no reports of a bladder-on-chip model. Although there are studies that have developed *in vitro* bladder models that recreate the stratified architecture of the bladder epithelium (Horsley et al., 2018; Smith et al., 2006; Suzuki et al., 2019), they have not been used to recapitulate the multiple stages of IBC formation. Similarly, while a few studies have visualized different stages of IBC development by culturing human bladder cells under urine flow, these models are restricted to monoculture experiments (Andersen et al., 2012; Iosifidis and Duggin, 2020). Furthermore, the lack of vasculature in these models restricts the extent to which immune cell components or drugs can be introduced in a physiologically relevant manner and none of the systems reported to date offer the possibility of mimicking the mechanics of filling and voiding in a functioning bladder (Andersen et al., 2012; Horsley et al., 2018; Iosifidis and Duggin, 2020; Smith et al., 2006).

Here we report the development and characterization of a bladder-chip model that mimics the bladder architecture by co-culture of a well-characterized human bladder epithelial cell line with bladder microvascular endothelial cells in a device geometry that allows the two cell types to be exposed to urine and nutritive cell culture media, respectively. The flow rates in the apical and vascular channels can be controlled independently, and multiple rounds of micturition are recreated via the application of a linear strain to the PDMS membrane that serves as the substrate for co-culture. Using this model, we show that diapedesis of neutrophils to sites of infection on the epithelial side can lead to the formation of neutrophil swarms and neutrophil extracellular traps (NETs), and that IBCs offer substantial protection to bacteria from antibiotic clearance. Our observations suggest that the role of IBCs in reseeding bladder infections upon cessation of antibiotic treatment or failure to complete a course of antibiotics might be more important than

104 previously assumed and therefore strategies aimed towards eradication of IBCs are very crucial
105 for treatment efficacy.
106

107 # Results

108 **Reconstitution of bladder uroepithelium and bladder vasculature**

109 We established a bladder-chip infection model by co-culturing HTB9 bladder epithelial cells
110 (epithelial cells) and HMVEC-Bd primary human bladder microvascular endothelial cells
111 (endothelial cells) in a novel bladder-chip approach (Fig. 1A). Immunostaining verified that the
112 epithelial and endothelial cells formed confluent monolayers (cell densities in Table 1) with high
113 expression of junction markers such as epithelial cell adhesion molecule (EpCAM) in the
114 epithelial cell layer, and platelet endothelial cell adhesion molecule-1 (PECAM-1) and VE-
115 cadherin in the endothelial cell layer (Fig 1B, C, additional images in Fig. S1A-H). Expression of
116 these and other junction markers such as E-cadherin and zonula occludens-1 (ZO-1) was
117 consistent across monocultures (Fig. S2A-G).
118

119 Similarly, a majority of the epithelial cells expressed cytokeratin 7 (CK7), a general uroepithelial
120 marker and cytokeratin 8 (CK8), a differentiated uroepithelial marker both in monoculture (Fig.
121 S2I, J) and on-chip (Fig. 1B, S1B, S1F). Some endothelial cells were also CK7+ (Fig. 1C, S2H).
122 Co-culture of bladder epithelial and bladder endothelial cells in the human bladder-chip therefore
123 did not alter the cellular expression patterns of these markers as compared to monocultures. We
124 further characterized the HTB9 cell line in monoculture for markers for urothelial differentiation.
125 HTB9 cells showed high expression of uroplakin-3a (UP3a) which has been shown to be
126 essential for UPEC infection (Fig. S2K) (Martinez et al., 2000; Mulvey et al., 1998) but only a

127 small proportion of epithelial cells were positive for the basal cell marker cytokeratin1 (CK1), in
128 agreement with the umbrella cell nature of the HTB9 cell line (Fig S2L, M) (Duncan et al., 2004;
129 Smith et al., 2006). Overall, these observations confirmed that the bladder-chip is populated with
130 cells that mimic the physiology of the bladder vasculature and the superficial urothelial cell
131 layer. Further, the chip design enables the flow of media with different compositions through the
132 epithelial and vascular channels. We used this feature to mimic bladder physiology by perfusion
133 of diluted pooled human urine on the epithelial side and endothelial cell medium on the vascular
134 side.
135
136 **Modelling bladder filling and bladder voiding in the bladder-chip**
137 The human bladder experiences vast changes in volume and surface area on a periodic basis. The
138 first phase of this cycle, ('*filling bladder* state'), occurs through a slow and gradual increase in
139 bladder volume due to addition of urine from kidney via the ureters, resulting in a large increase
140 in bladder volume (Fig. 1D). At the level of the uroepithelium, these changes manifest as a 2-
141 dimensional biaxial stretch of the bladder tissue. *Ex vivo* studies in rat bladders report that a
142 maximum strain of 90% and 130% can be applied to bladder explants in the circumferential and
143 longitudinal directions (Gloeckner et al., 2002; Parekh et al., 2010), although micturition *in vivo*
144 is likely triggered before this maximum value is reached. Subsequently, volume growth slows,
145 and the bladder attains a relatively constant volume, with the bladder epithelium in a
146 corresponding state of maximal stretch, ('*filled bladder* state'). Voiding of the bladder through
147 urination rapidly reduces bladder volume, ('*voiding bladder* state') and removes the strain
148 experienced by the bladder cells. The bladder epithelium, as a viscoelastic material, responds to

149 the removal of strain and relaxes over the subsequent period (Pascalis et al., 2018) where the
150 bladder volume remains low ('*voided bladder* state') (Fig. 1D).
151 The architecture of the bladder-chip device allows for a linear strain to be applied to the porous
152 membrane via negative pressure in the channels adjacent to the main channel of the device ('the
153 vacuum channels') (Grassart et al., 2019; Huh et al., 2010b) (Fig. 1A). We characterized the
154 linear strain experienced by epithelial cells due to application of negative pressure (Fig. S3). A
155 plot of applied pressure vs. strain was linear, and we could achieve a dynamic range of linear
156 strain (0 to 19 %) by application of negative pressure (0 to -900 mbar). High levels of applied
157 strain were incompatible with long-term time-lapse microscopy as it generated a significant drift
158 in the axial position of the membrane. We therefore limited the linear strain applied to a
159 maximum of 10%, which is nevertheless a significant proportion of the typical strain experienced
160 by the bladder tissue *in vivo*. We then modelled the bladder filling and voiding over a 6-hour
161 duty cycle with different states: *filling bladder* (0 to 2 hours, 0 to 10% strain), *filled bladder* (2 to
162 4 hours, 10% strain), *voiding bladder* over a period of 2 minutes (4 hours to 4:02 hours, 10% to
163 0% strain) and *voided bladder* (4:02 hours to 6 hours, 0% strain) (Fig. 1D). This 6-hour duty
164 cycle was then repeated for the remaining duration of each experiment. Overall, the bladder-chip
165 model enables co-culture of two cell-types in nutritionally different microenvironments with a
166 physiologically relevant level of applied strain that mimics bladder filling and voiding cycles.
167

168 **UPEC infection of the epithelial layer under flow in the bladder-chip model**

169 UPEC attachment and invasion of bladder epithelial cells has been shown to be sensitive to
170 fluidic shear stress (Andersen et al., 2012; Zalewska-Piątek et al., 2020). Although UPEC
171 infection in the bladder can occur with or without the presence of shear stress, we infected the

172 epithelial layer on the bladder-chip under flow conditions. The small volumes of the microfluidic
173 chip motivated this approach, as rapid bacterial growth in the diluted human urine could lead to
174 acidification of the medium. We therefore maintained a flow rate of 1.2 ml/hour for a period of
175 1.5 - 2 hours during infection of the epithelial layer of the bladder-chips with UPEC. Under flow
176 conditions, an overwhelming majority of bacteria did not attach to the epithelial cells. Time-
177 lapse microscopy showed that bacterial attachment to the epithelial cells increased steadily over
178 this period, but that the typical infectious dose at the end of this period was low (<1 bacterium
179 per epithelial cell, Fig. S4).
180
181 Accordingly, we established a 28-hour live-cell imaging experimental protocol as shown in the
182 schematic in Fig. 1E and described in greater detail in the subsequent sections and in the
183 Materials and Methods. Briefly, this consisted of an initial period of acclimatization, followed by
184 UPEC infection, introduction of neutrophils, and two consecutive cycles of antibiotic treatment
185 and recovery to monitor IBC dynamics at the single-cell level. This experimental protocol
186 therefore mimicked key aspects of the host-pathogen interactions in early stages of UTIs as well
187 as the response to antibiotic treatment.
188
189 **Diapedesis of neutrophils across the epithelial-endothelial barrier in response to UPEC**
190 **infection in the bladder-chip**
191 The bladder-chip platform enables continuous imaging while maintaining flow in both epithelial
192 and vascular channels and mechanically stretching the membrane as part of the bladder voiding
193 cycle. At the start of each live-cell imaging experiment, bladder epithelial cells in an initial
194 relaxed state were perfused with sterile pooled human urine diluted in PBS on the epithelial side

195 and endothelial cell medium on the vascular side respectively (Fig. 2A1, B1, S5A1). The
196 epithelial side was inoculated with a low dose of UPEC in diluted urine and infection was
197 performed under flow (Fig. 2A2, B2, S5A2) for ca. 1.5 to 2 hours. The first bladder duty cycle
198 also initiated at this timepoint. We maintained the optical focus of the microscope on the
199 epithelial layer over the subsequent course of infection. UPEC attachment was evident during
200 this infection phase by visual inspection (Fig. 2B2, S5A2).
201 After this period of infection, unattached bacteria in the epithelial channel were removed by
202 perfusion of diluted urine. Our aim was to study the interaction of UPEC with host cells,
203 therefore this perfusion was maintained throughout the experiment. Continuous perfusion
204 reduced the accumulation of bacteria in the urine and enabled imaging of intracellular bacteria
205 without large background noise in the fluorescence channels from planktonic bacteria. We
206 subsequently performed a series of interventions that mimic the course of UTI infections and
207 used time-lapse imaging to monitor the simultaneous changes in host-pathogen interaction
208 dynamics. To mimic the host response, immune cells were introduced into the vascular channel.
209 Among innate immune cells, neutrophils are the first line of defense in UTIs (Haraoka et al.,
210 1999). We isolated neutrophils from human blood and verified that the isolation procedure
211 yielded neutrophils with a high degree of purity (Son et al., 2017) through immunostaining for
212 CD15, a neutrophil specific marker (Zahler et al., 1997) (Fig. S6). To enable identification and
213 tracking of neutrophils, they were pre-labelled with CellTracker™ Deep Red dye, which stains
214 the cytoplasm of these cells.
215 Neutrophils were subsequently introduced in the bladder-chip devices through the vascular
216 channel, mimicking the natural route of immune cell migration into the bladder (schematic in
217 Fig. 2A3-A5, snapshots in Fig. 2B3-B5, S5A3-A5). We used a cell concentration of ca. 2 million

218 cells/ml similar to the neutrophil concentration in human blood (Hsieh et al., 2007). During this
219 period, the flow rate through the vascular channel was increased to 3ml/hour to provide a shear
220 stress η= 1 dyne/cm^2, which aids neutrophil attachment to endothelial cells (Alon et al., 1995). In
221 uninfected control chips, neutrophil attachment to the endothelial layer was minimal (Fig. S7A,
222 B) and diapedesis of neutrophils to the epithelial layer was rare (Fig. 2C, S8A). In stark contrast,
223 infection of the epithelial layer with UPEC elicited a robust attachment of neutrophils to
224 endothelial cells (Fig. S7C, D), along with rapid diapedesis across to the epithelial side (Fig.
225 2B2-B4, S5A2-A4, S8C). We confirmed that neutrophil diapedesis was also stimulated in the
226 absence of infection, upon exposure to a gradient of pro-inflammatory cytokines that are
227 typically upregulated during UTIs (Agace et al., 1993; Hedges et al., 1992; Nagamatsu et al.,
228 2015; Song et al., 2007) (interleukin-1α, interleukin1-β, interleukin-6 and interleukin-8 each at
229 100 ng/ml) across the epithelial-endothelial barrier (Fig. S8B). However, neutrophil diapedesis
230 was more robust upon infection as compared to the cytokine gradient, with a higher number of
231 neutrophils observed across multiple fields of view on the epithelial side (Fig. S8B-D). These
232 results suggest that infection on-chip generates a strongly pro-inflammatory environment locally
233 and that neutrophil diapedesis is further stimulated by the presence of UPEC (Agace et al., 1995;
234 Oliveira et al., 2016).
235
236 Using time-lapse imaging, we were also able to quantify the kinetics of neutrophil migration
237 with a temporal resolution of up to 7.5 minutes. Neutrophil diapedesis to the epithelial sites of
238 infection was detected as early as ca. 15-17 minutes post-introduction into the vascular channel
239 (Fig 2B3, S5A3, supplementary movie SMov1, SMov2). Neutrophils that migrated to the
240 epithelial side aggregated on the epithelial cells (Fig 2B4-2B5, S5A4-A5, supplementary movie

241 SMov1, SMov2) In some cases, these neutrophils were able to control bacterial growth (Fig.
242 2B4-2B5, solid yellow boxes) whereas in others, bacterial growth was uncontrolled (Fig. 2B4-
243 2B5, dashed white boxes). Diapedesis was observed in every field of view examined across n=4
244 infected chips, whereas diapedesis occurred infrequently in uninfected controls (Fig. 2C).
245 Furthermore, the size of these aggregates was significantly larger in infected bladder-chips vs.
246 uninfected controls, with the aggregates in case of infected-chips exhibiting the characteristic
247 features of neutrophil swarms (Kienle and Lämmermann, 2016; Kreisel et al., 2010;
248 Lämmermann et al., 2013). We quantified the size of the swarms formed by either estimating the
249 maximum number of neutrophils observed in fields of view on the epithelial side (Fig 2D) or by
250 measuring the total volume occupied by neutrophils normalized to the volume of a 3D field of
251 view (Fig 2E). Using either metric, infection generated large swarms that did not occur in
252 uninfected bladder-chips. The dynamics of swarm formation across n=51 and n=40 fields of
253 view in two infected bladder-chips are shown in Fig. 2F. In infected bladder-chips, swarm
254 formation was rapid, and swarms reached their maximum size typically between 60- and 90-
255 minutes post-introduction of neutrophils (Fig. 2G).
256
257 **Neutrophil extracellular traps (NETs) formation in response to UPEC infection**
258 Neutrophils have complex responses to infections (Oliveira et al., 2016), including the formation
259 of neutrophil extracellular traps (NETs) that occur by the release of cytosolic azurophilic
260 granules around a scaffold of decondensed chromatin and potentially serves to trap and kill
261 extracellular bacteria (Brinkmann et al., 2004). NETs have been shown to consist of
262 antimicrobial granules such as myeloperoxidase (Metzler et al., 2011) and neutrophil elastase
263 (Papayannopoulos et al., 2010) and have been observed in urine harvested from UTI patients (Yu

264 et al., 2017). Interestingly, we observed NET formation by neutrophils in the infected bladder-
265 chip. We verified the formation of NETs on the epithelial layer through immunostaining of
266 infected bladder-chips at 3.5 hours post-infection and 2 hours post-introduction of neutrophils in
267 the vascular channel using antibodies against neutrophil myeloperoxidase (Fig 2H, S9A1-A3)
268 and neutrophil elastase (Fig 2I, S9B1-B3). In each case, areas on the epithelial layer with strong
269 immunostaining were observed (Fig. 2H3, 2I3). Neutrophils in these areas were typically in large
270 numbers, characteristic of swarms. In addition, by this stage of the experiment, neutrophils that
271 had high levels of myeloperoxidase or elastase typically did not retain strong expression of the
272 cytoplasmic CellTracker dye used for identification of neutrophils in live imaging (cf. Fig. 2H2
273 and 2H3, 2I2 and 2I3). For each example, a zoomed-in image clearly shows long filament-like
274 structures that extend between cells and are either myeloperoxidase positive (Fig. 2H5) or
275 neutrophil elastase positive (Fig. 2I5), strongly suggestive of NETs (Brinkmann et al., 2004;
276 Metzler et al., 2011; Papayannopoulos et al., 2010). NET formation was also observed in some
277 instances by neutrophils in some locations on the endothelial channel, although large swarms did
278 not form here (Fig. S9B1-B3).
279 To further characterize these structures, we imaged the epithelial layer of uninfected and infected
280 bladder-chips with or without the addition of neutrophils using scanning electron microscopy
281 (SEM). Representative images of the epithelial layers of uninfected bladder-chip controls (Fig.
282 S10A) contrast with those from infected bladder-chips after neutrophil diapedesis (Fig. 2J1-J4,
283 S10C) and clearly highlight the distinctive features of NET formation. In Fig. 2J1, neutrophils on
284 the surface of the epithelial layer are clearly distinguishable by their distinctive spherical
285 morphology and size (amber arrowheads). Thick bundles consisting of many thinner NETs
286 formed between these neutrophils are shown by white arrowheads and appear to extend between

287 adjacent neutrophils, as is also evident in Fig. S10C. A majority of the epithelial cells have a
288 characteristic flattened morphology with cell appendages that can extend between cells (cyan
289 arrowheads); an example of a highly infected epithelial cell that is spherical in shape and with
290 bacteria attached to its surface is indicated with a purple arrowhead (Fig. 2J1). A series of
291 higher-magnification images in Fig. 2J2-2J4 show the structure of NETs in greater detail. Many
292 individual UPEC bacteria (green arrowheads) are captured in these NETs (Fig. 2J2-2J4), which
293 are themselves composed of many individual thinner fibres (indicated by yellow arrowheads in
294 Fig. 2J2-2J4). These structures did not form in infected bladder-chips without the introduction of
295 neutrophils (Fig. S10B), confirming their identity as structures identified as NETs via
296 immunofluorescence (Fig. 2H, I). NET formation was a direct response to UPEC and not caused
297 by hyperactivation of neutrophils due to experimental handling. To verify this, we collected the
298 neutrophils that passed through an infected bladder-chip without attachment. Even upon
299 infection, an overwhelming majority of the cells perfused into the chip flow out without
300 adhering, because of the geometry of the channels in the device. NET formation in these samples
301 was not observed unless the neutrophils were themselves infected by UPEC shed from the
302 bladder-chip (Fig. S11). The bladder-chip model is therefore able to recapitulate key aspects of
303 the host response to the early stages of UPEC infection while demonstrating that intracellular
304 bacteria were substantially protected from neutrophil-mediated killing.
305
306 **Heterogenous dynamics of intracellular bacterial communities within urothelial cells**
307 Urinary tract infections that do not resolve upon intervention by the host immune system often
308 require treatment with antibiotics. Antibiotics have complex pharmacokinetic and
309 pharmacodynamic profiles *in vivo*, which we attempted to model through two successive rounds

310 of high dose administration of antibiotics (ampicillin at 40x MIC, Fig. S12A), on both the
311 epithelial and vascular side, interrupted by periods with no antibiotic (schematics in Fig. 3A, 1E).
312 Continuous time-lapse imaging over this entire period allowed us to capture the responses of
313 bacteria to this simplified model of antibiotic profiles and to study the persistence of UPEC upon
314 antibiotic treatment in the different physiological niches (Fig. 3 and Fig. 4).
315 A consequence of the first cycle of antibiotic administration under flow was the elimination of
316 planktonic bacterial growth in the media in the apical channel, as is observed within the lumen of
317 the bladder *in vivo*. Many bacteria that were still intact at the end of the antibiotic treatment
318 intact did not regrow after the antibiotic was removed (Fig. S12 B). Regrowth commenced in
319 only a small fraction of bacteria (Fig. S12C) after a variable lag phase (Fig. S12D) and rapid
320 regrowth was highly correlated with intracellular location of bacteria within epithelial cells.
321 These subsequently proceeded to form intracellular bacterial communities (IBCs), with a
322 variable lag period. An example of an early stage of the IBC formation is shown in the timeseries
323 in Fig. 3B1-B5, supplementary movie SMov3. This IBC was initially seeded with few bacteria
324 that are present in Fig. 3B1 and clearly visible in Fig. 3B2. At the end of the timeseries, the
325 entire host cell was packed with bacteria (Fig. 3B5). The exponential increase in bacterial
326 numbers frequently led to the saturation of the 8-bit images in the bacterial channel. We
327 therefore examined similar structures in separate bladder-chips via immunofluorescence (Fig.
328 3C, S13) staining. Zooms of two of the four IBCs highlighted in Fig. 3C show numerous tightly
329 packed bacteria within epithelial cells that are both CK7+ (Fig. 3C) and CK8+ (Fig. S13). These
330 bacterial morphologies are highly similar to early-stage IBCs observed in the bladder (Anderson
331 et al., 2003; Duraiswamy et al., 2018; Justice et al., 2004). Higher resolution images of the
332 biofilm-like structures within IBCs obtained via correlative light (Fig. 3D) and transmission

333 electron microscopy (Fig. 3E) showed that bacteria in IBCs can be either coccoid or rod shaped,
334 which is also evident in scanning electron micrographs of bacteria within IBCs (Fig. 3F). IBCs
335 within bladder-chip model therefore show many of the distinctive morphological features
336 reported from images of infected bladders in the mouse model (Anderson et al., 2003; Hunstad
337 and Justice, 2010).
338
339 Numerous reports from the mouse model of infection have shown IBCs to be dynamic structures;
340 growth in IBCs eventually culminates in bacterial shedding or the complete exfoliation of the
341 IBC. The underlying dynamics of these phenotypes is hard to capture in the mouse model, but
342 the bladder-chip model allowed us to track the dynamics of bacterial growth within individual
343 IBCs over extended periods of time, providing information on bacterial dynamics within so-
344 called early, middle, and late-stage IBCs. An example of the heterogeneity in growth rates is
345 evident from the timeseries for three IBCs in Fig. 3G1-G5, supplementary movie SMov4.
346 IBCs#1 and 2 subsequently began to shed individual bacteria (Fig. 3G4), a phenotype not
347 observed in IBC#3. At a later timepoint (Fig. 3G5) the fates of all three IBCs were dramatically
348 different – the cell containing IBC#1 had completely exfoliated and was removed from the field
349 of the view by flow in the epithelial channel, IBC#2 continued to shed bacteria, whereas growth
350 remained slow in IBC#3. We monitored the eventual fate of n=100 IBCs during the first and the
351 second growth cycles which confirmed that shedding and exfoliation were not mutually
352 exclusive. While some IBCs only shed bacteria (n=28) and others exfoliated without shedding
353 (n=27), a substantial fraction of IBCs showed shedding prior to exfoliation (n=31) and some
354 IBCs displayed neither phenotype (n=14). Furthermore, in addition to the coccoid and rod-
355 shaped morphologies highlighted in Fig. 3C-F, time-lapse imaging also enabled us to capture

356 morphotypes that occurred relatively rarely such as the intracellular growth of filamentous forms
357 of UPEC (Fig. 3H1-H5, S14, supplementary movie SMov5, SMov6). In this time series, a
358 filamentous bacterium can be seen and appears to encircle the inner boundary of the cell (Fig.
359 3H1-3H4) before filling the volume entirely (Fig. 3H5). Overall, time-lapse imaging confirms
360 that a significant fraction of bacteria within IBCs can survive the first round of antibiotic
361 treatment and are the source for reseeding of both the extracellular bacterial populations as well
362 as the subsequent growth of IBCs in newly infected cells.
363

364 **Dynamic persistence of intracellular bacterial communities within uroepithelial cells**

365 A subsequent round of antibiotic treatment provided an opportunity to study the dynamic
366 persistence of bacteria within IBCs in response to an antibiotic profile that was a closer mimic of
367 the periodic antibiotic exposures *in vivo*. Furthermore, at this stage of the experiment, we were
368 also able to study the responses of bacteria in intermediate and mature late-stage IBCs to
369 antibiotic treatment, which was not possible during the first round of antibiotic administration
370 early in the course of infection. In the examples highlighted in Fig. 4A1-A5 and supplementary
371 movie SMov7, bacterial growth after the first round of antibiotic treatment resulted in the
372 formation of many large IBCs with tightly packed bacteria (Fig. 4A1-A2). Many of the bacteria
373 within each of the four IBCs were eliminated by the antibiotic, but a substantial proportion of
374 bacteria in each IBC nevertheless survived the antibiotic treatment (Fig. 4A3). Each of these
375 IBCs subsequently regrows when the antibiotic is removed (Fig. 4A4-A5), and two additional
376 IBCs are seeded during this time (white arrowheads in Fig. 4A5). Overall, the second round of
377 antibiotic administration led to a sharp decline in instances of subsequent bacterial regrowth (Fig.
378 S12C). In all instances, regrowth either occurred directly within IBCs, or was caused by the

379 shedding of bacteria from IBCs to repopulate the extracellular niche and seed new IBCs,
380 highlighting the dynamic stability of this niche and its importance in establishing persistent
381 infection. We therefore performed a careful analysis to quantify bacterial growth rate within
382 IBCs. Growth within IBCs across different time periods was exponential (Fig. 4B). We were
383 able to track a subset of IBCs across two growth cycles (examples in Fig. 4C). In a majority of
384 instances these revealed exponential growth in the absence of antibiotic, delayed response to
385 antibiotic, and a lag phase after the antibiotic was removed. In general, bacterial growth in IBCs
386 in the second growth cycle was slower than in the first (Fig. 4D). However, this population level
387 statistic may be influenced by the fact that many of the IBCs monitored in the second growth
388 cycle had been exposed to two rounds of antibiotic treatment. For this sub-population, in n=16
389 out of n=18 IBCs, growth was slower after the second round of antibiotic administration (Fig.
390 4E).
391 Next, we examined the dynamics of bacterial growth within IBCs during the period of antibiotic
392 treatment in greater detail. In the IBC shown in the timeseries in (Fig. 4F1-4F5, S15A1-A5,
393 supplementary movie SMov8, SMov9), growth before antibiotic administration (Fig. 4F1, 4F2)
394 continued for a considerable period after the antibiotic was administered (Fig. 4F3, Fig. 4F4,
395 S15A1-S15A3). Eventually, a reduction in bacterial volume towards the end of the antibiotic
396 administration period was observed (Fig. 4F5, S15A4-S15A5). In contrast, the relatively smaller
397 IBC in the timeseries in Fig. 4G1-4G5, S15B2-S15B5, supplementary movie SMov10, SMov11
398 continued to grow throughout the period of antibiotic administration. These different dynamics
399 are also captured in the plot of bacterial volume for multiple IBCs before, during, and after the
400 antibiotic treatment (Fig. 4H). In all cases, bacterial volume continues to increase during a
401 significant period of antibiotic administration and in 2 out of 18 cases, there was no decrease in

402 bacterial volume throughout this period (Fig. 4H). In contrast, extracellular bacteria likely
403 adherent on the epithelial cells but not internalized within them were rapidly eliminated by
404 combination of antibiotic treatment and flow (Fig. 4I), in all cases the bacterial volume reduced
405 immediately upon antibiotic administration. This differential killing resulted in a significantly
406 higher proportion of extracellular population of bacteria being killed (Fig. 4J). Elimination of
407 bacteria within IBCs was highly heterogenous. Another consequence of this differential killing
408 was that after the second round of antibiotic treatment, regrowth was observed in only a very
409 small fraction of non-IBC UPEC (Fig. S12C). Protection of bacteria within IBCs therefore has a
410 direct outcome of enabling the reseeding of infection at other locations within the epithelial
411 monolayer.
412
413 Lastly, we sought to determine if the bladder duty cycle altered the dynamics of UPEC infection.
414 A comparison between infected bladder-chips with and without the duty cycle (Fig. 4K, L, S16)
415 revealed a significant increase in the bacterial burden when the duty cycle was implemented
416 (Fig. 4M). These results suggest that the bladder filling and voiding cycle influence the uptake
417 and proliferation of UPEC, possibly through physiological changes in the epithelial cells in
418 response to applied strains (Apodaca, 2004; Carattino et al., 2013; Truschel et al., 2002; Wang et
419 al., 2005). In turn, they suggest a deeper connection between the physiology of mechanically
420 active organs such as the bladder and the processes of infection, which can be characterized in
421 detail using this bladder-chip model.
422

423 **Discussion**

424 In our human bladder-chip model, we focused on recapitulating the key aspects of bladder
425 physiology relevant to the study of the earliest stages of UPEC infection and IBC formation.
426 Therefore, superficial bladder epithelial cells, the first cell-type usually infected by UPEC, were
427 cultured both under flow in diluted pooled urine and in co-culture with bladder microvascular
428 endothelial cells. The ability to apply a cyclic mechanical stretch to the PDMS membrane,
429 originally designed to mimic the breathing motion in the lung (Huh et al., 2010b) or the
430 peristaltic motion in the gut (Kim and Ingber, 2013), has been adapted here to mimic the slow
431 expansion and rapid contraction of bladder volume. We demonstrate the ability to perform
432 multiple duty cycles while simultaneously imaging the infected device via long-term time-lapse
433 imaging, a technical advance that is difficult to achieve with bladder explants (Justice et al.,
434 2004) or other *in vitro* studies of UPEC infection of bladder epithelial cells (Andersen et al.,
435 2012; Horsley et al., 2018; Iosifidis and Duggin, 2020; Smith et al., 2006). Using this approach,
436 we found that the total bacterial burden inside infected bladder-chips was significantly higher at
437 a late stage of infection if a duty cycle was applied, unlike the non-significant influence of cyclic
438 stretching on Shigella infection of intestinal-chips under flow conditions (Grassart et al., 2019).
439 The exact mechanisms underlying this phenomenon remain to be explored, but there is an
440 increasing understanding of the role of mechanical forces in regulating innate immune function
441 (Solis et al., 2019). Our results showcase the ability of the bladder-chip model to capture these
442 interactions between mechanical function, physiology, and infection, unlike other infection
443 models reported thus far.

444 A primary focus of *in vitro* models developed so far has been to probe specific aspects of UPEC
445 infection, such as the role of the stratified bladder architecture (Horsley et al., 2018) or the
446 effects of micturition on IBC formation (Andersen et al., 2012; Iosifidis and Duggin, 2020).

447 However, the migration of immune cells into the bladder is difficult to reproduce in these
448 models, and in many of these systems, live-cell imaging remains technically challenging
449 (Horsley et al., 2018; Smith et al., 2006). Furthermore, the models do now allow mechanical
450 manipulations of the cellular co-culture. In that sense, the bladder-chip model complements these
451 existing approaches by providing these additional functionalities. Further development,
452 potentially through the combination of organoid and organ-on-chip approaches, could lead to the
453 development of a fully stratified uroepithelium on-chip.
454
455 Neutrophils are the first responders to UPEC infection (Abraham and Miao, 2015; Haraoka et al.,
456 1999), and neutrophil migration involves a series of steps that commences with attachment to the
457 endothelium under flow, migration on the endothelial surface, diapedesis across the epithelial-
458 endothelial cell barrier and movement towards the site of infection (Ley et al., 2007; Nourshargh
459 et al., 2010). Perfusion of the vascular channel with CD15+ neutrophils isolated from human
460 blood shows that the bladder-chip model recapitulates all these phenotypes, with rapid diapedesis
461 of neutrophils to sites of infection. There, neutrophils aggregate to form swarms (Hopke et al.,
462 2020; Kienle and Lämmermann, 2016; Lämmermann et al., 2013; Reátegui et al., 2017) and
463 subsequently, the formation of NETs (Branzk et al., 2014; Brinkmann et al., 2004; Metzler et al.,
464 2011; Papayannopoulos et al., 2010) around extracellular bacteria is observed. Characterization
465 of these structures via SEM shows that they can extend across many tens of microns and stain
466 positive for myeloperoxidase (Metzler et al., 2011) and neutrophil elastase (Papayannopoulos et
467 al., 2010), indicative of potent anti-microbial activity. However, neutrophil control of infection
468 on-chip is partial; this is possibly due to the unrestricted growth of large numbers of extracellular
469 bacteria and in some instances, exacerbated by the loss of some neutrophils due to flow in the

470 channel. Another contributing factor could potentially be the architecture of the PDMS
471 membrane, which permits neutrophil diapedesis only at fixed spatial locations on-chip.
472 Neutrophil migration may also be impacted by the relative stiffness of the PDMS membrane.
473 Nevertheless, the demonstration of NET formation is consistent with the occurrence of these
474 structures both in the mouse model (Ermert et al., 2009) as well as in the urine of infected
475 patients (Yu et al., 2017) and suggests that the model is able to recapitulate important aspects of
476 disease. It is also an important advance for the use of organ-on-chip approaches to recapitulate
477 NET formation in infectious diseases.
478
479 IBC formation begins immediately after infection and is already underway upon neutrophil
480 administration. However, clear demonstration of IBCs with a high degree of confidence was only
481 possible after an initial treatment with a high dose of antibiotic that eliminated extracellular
482 planktonic bacteria and improved the optical imaging of bacteria attached to or within epithelial
483 cells. It enabled us to capture the full cycle of IBC growth from few bacteria to a large biofilm
484 and subsequent release via shedding and filamentation. Importantly, the compact nature of the
485 device allowed us to image multiple IBCs concurrently on the same chip with a high temporal
486 resolution while simultaneously mimicking the bladder filling and voiding cycles, which is
487 difficult to achieve in bladder explants (Justice et al., 2004) or bladder monoculture *in vitro*
488 model systems (Andersen et al., 2012; Iosifidis and Duggin, 2020). Our observations reiterate the
489 highly dynamic nature of these structures; growth was asynchronous and heterogenous and
490 outcomes included bacterial shedding, exfoliation and filamentation (Hunstad and Justice, 2010;
491 Justice et al., 2004; Scott et al., 2015). Notably, shedding and exfoliation were not mutually

492 exclusive for the time-period of our observations – we report examples of IBCs that shed
493 bacteria and contract in volume before exfoliation.
494
495 While IBCs are clearly acknowledged as critical players in early infection, the contribution
496 towards promoting persistence is not completely understood. For example, Blango *et al*.,
497 (Blango and Mulvey, 2010) showed that incubation of bladder explants containing IBCs with a
498 high dose of antibiotics for a period of 18 hours resulted in a substantial sterilization of these
499 structures and concluded that other populations, notably quiescent reservoirs (Mysorekar and
500 Hultgren, 2006) might play a greater role in the establishment of persistent populations.
501 However, the pharmacokinetic profiles of most antibiotics in the host are not time invariant. In
502 case of ampicillin, a standard regimen of ampicillin treatment is typically a bolus of 250-500 mg
503 of antibiotic administered every 6 hours. Within the serum, ampicillin concentration peaks at a
504 C_{max} ~ 3-40 μg/ml, which is between 1.5 to 20-fold the MIC as measured in human serum
505 (Bryskier, 2020; Putrinš et al., 2015). We therefore chose concentrations that captured these
506 antibiotic exposures (we used ampicillin at 40x MIC measured in the endothelial cell medium
507 perfused in the vascular channel). Ampicillin concentrations in the blood rapidly decay with a
508 half-life of between 60 and 90 minutes with a characteristic pharmacokinetic/pharmacodynamic
509 profile. This period is modelled well by our experimental protocol where phases with high
510 concentration of ampicillin are interspersed with periods with no antibiotic. We are therefore
511 able to model the delivery of two consecutive doses of antibiotic and find that IBCs offer
512 substantial protection against sterilization by a short duration of a high-dose antibiotic treatment
513 and in many instances, bacterial regrowth after two successive rounds of antibiotic
514 administration. Notably, in smaller 'early IBCs', bacterial growth continues throughout the

515 period of ampicillin administration, suggesting that the intact nature of the cell membrane likely
516 diminishes the effect of the drug. Our results suggest that, IBCs may continue to play a role in
517 reseeding sites of infection for a considerable period after the commencement of antibiotic
518 treatment. This has particularly important implications with regard to the compliance of
519 antibiotic use as proliferating IBCs could rapidly re-seed sites of infection throughout the bladder
520 if antibiotic doses are missed. These unique capabilities of the bladder-chip to realistically model
521 antibiotic treatment regimens for IBCs can be leveraged in the future to screen compounds
522 (Spaulding et al., 2017) and identify optimal antibiotic treatments regimens that can eliminate
523 persistent bacterial populations in IBCs or alter the host-pathogen interaction dynamic in UTIs.
524
525 In summary, the bladder-chip model incorporates aspects of bladder physiology highly relevant
526 to early UPEC infection in a platform amenable to long-term live-cell imaging as well as for the
527 administration of antibiotics and therapeutics in a physiologically relevant manner. Our results
528 establish the suitability of this model for immunological and drug-delivery studies and show that
529 IBCs are highly dynamic structures that offer substantial protection from antibiotic clearance for
530 an extended period of time.
531

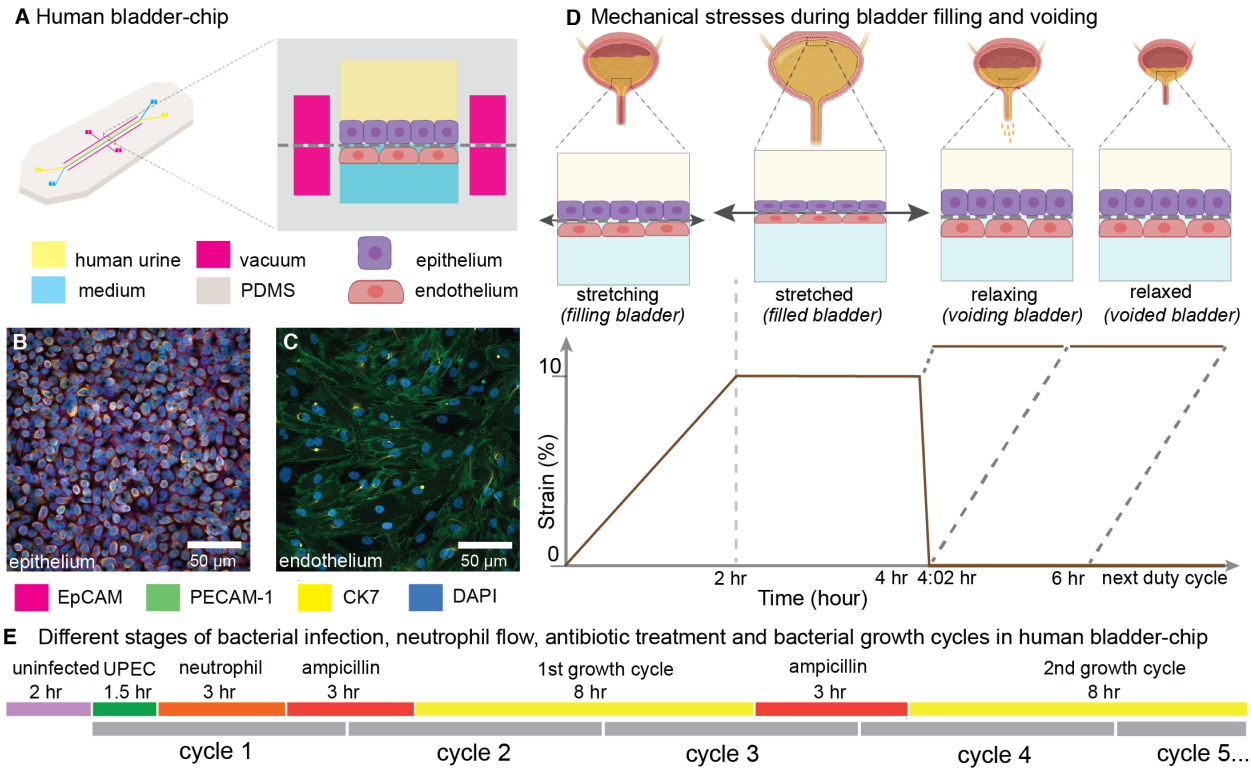

Figure 1: Human Bladder-chip model of UTI recapitulates the physiology of bladder filling and voiding.

(A) Schematic of the human bladder-chip with co-culture of the HTB9 human bladder epithelial cell line (epithelium, top) and primary human bladder microvascular endothelial cells (endothelial, bottom) on either side of the stretchable and porous membrane. Pooled human urine diluted in PBS and endothelial cell medium were perfused in the apical and vascular channels respectively to mimic bladder physiology. A negative pressure in the 'vacuum' channels (magenta) on either side of the main channel was applied to stretch the porous membrane to mimic stretching of the bladder. (**B**, **C**) Immunofluorescence staining of confluent epithelial and endothelial cell monolayers (anti-EpCAM (magenta) and anti-CK7 (yellow) for the epithelial cells and anti-PECAM-1 (green) for the endothelial cells) in an uninfected control chip. Some endothelial cells also stained positive for CK7. Cell nuclei were labeled with DAPI (azure). (**D**) Schematic of the reconstitution of the bladder filling and voiding cycle via stretching of the membrane with a duty cycle of 6 hours. The cycle consisted of a linear increase in strain through

547 stretching of the membrane (*filling bladder*, 0 to 2 hours), maintenance of the membrane under
548 stretch (*filled bladder*, 2 to 4 hours), a quick relaxation of applied strain over 2 minutes (*voiding*
549 *bladder*, 4:02 hours) and maintenance without applied strain (*voided bladder*, 4:02 hours to
550 6hours). (**E**) An overview of the timeline of the experimental protocol including infection,
551 addition of neutrophils via the vascular channel, and two cycles of antibiotic treatment
552 interspersed by two bacterial growth cycles. The consecutive bladder duty cycles are indicated.
553

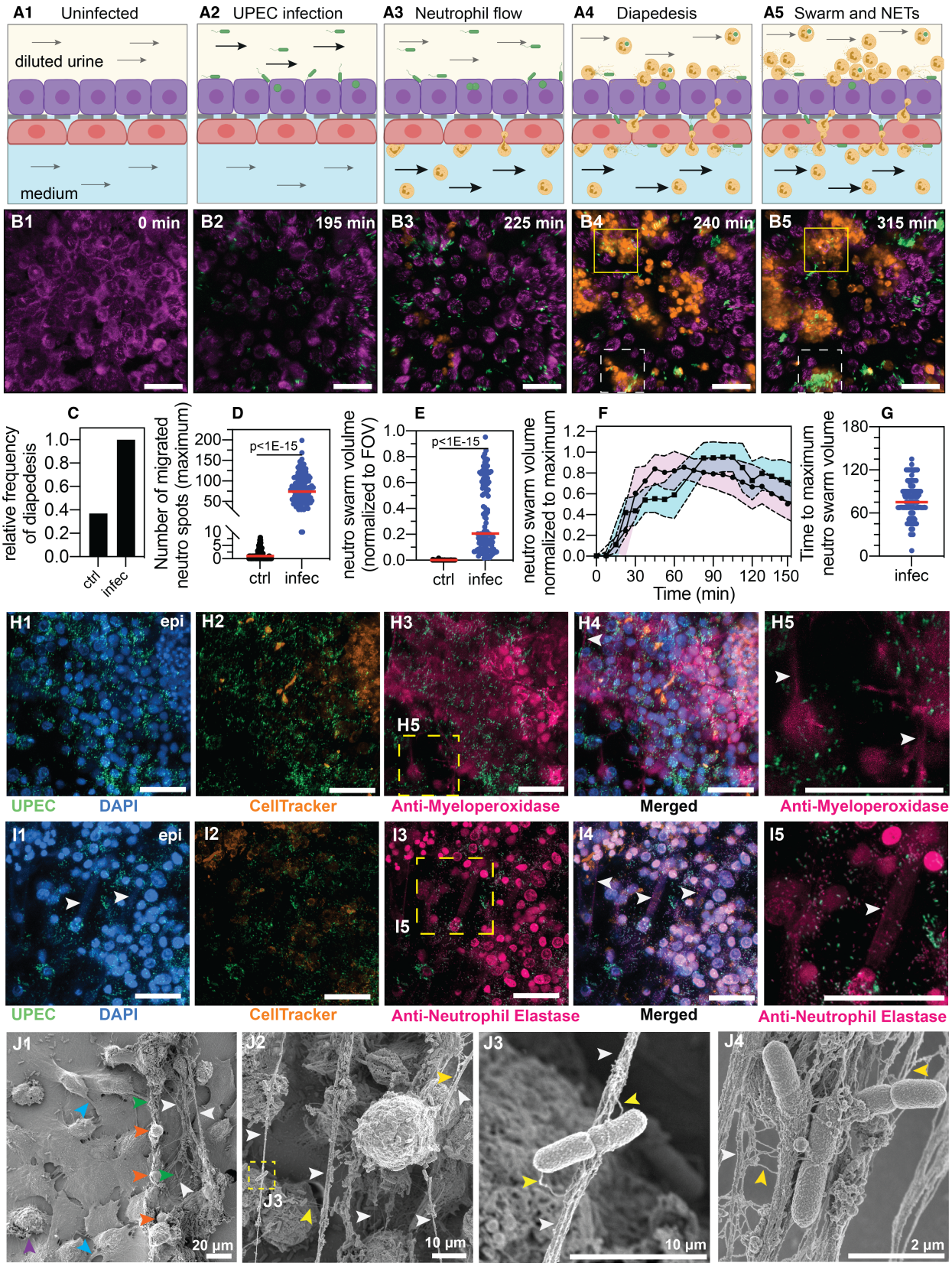
A1 Uninfected
A2 UPEC infection
A3 Neutrophil flow
A4 Diapedesis
A5 Swarm and NETs
diluted urine
medium
B1 0 min
B2 195 min
B3 225 min
B4 240 min
B5 315 min
C
relative frequency of diapedesis
ctrl
infec
D
Number of migrated neutro spots (maximum)
p<1E-15
ctrl
infec
E
neutro swarm volume (normalized to FOV)
p<1E-15
ctrl
infec
F
neutro swarm volume normalized to maximum
Time (min)
G
Time to maximum neutro swarm volume
infec
H1 epi
H2
H3
H4
H5
UPEC
DAPI
CellTracker
Anti-Myeloperoxidase
Merged
Anti-Myeloperoxidase
I1 epi
I2
I3
I4
I5
UPEC
DAPI
CellTracker
Anti-Neutrophil Elastase
Merged
Anti-Neutrophil Elastase
J1
J2
J3
J4
20 µm
10 µm
10 µm
2 µm

554
555

556 **Figure 2: Neutrophil diapedesis and NET formation on-chip.**

557 (**A1-A5**) Schematic of the UPEC infection, introduction of neutrophils and diapedesis of
558 neutrophils across the epithelial-endothelial barrier to sites of infection. Flow in the epithelial
559 and endothelial channels is indicated by arrows; the flow rate was increased upon introduction of
560 neutrophils in the vascular channel to increase attachment. (**B1-B5**) Snapshots from time-lapse
561 imaging highlighting each stage in the infection cycle shown in (**A1-A5**). Bladder epithelial cells
562 (magenta) and neutrophils (amber) were identified with membrane (Cell Mask Orange) and
563 cytoplasmic (Cell Tracker Deep Red) dyes, respectively. UPEC identified via constitutive
564 expression of YFP are shown in green. Neutrophil swarms could either control bacterial growth
565 (yellow dashed square, compare **B4** vs **B5**) or did not manage to restrict bacterial growth (white
566 dashed square, compare **B4** vs **B5**). (**C**) Bar charts for relative frequency of neutrophil diapedesis
567 (black) in n=3 uninfected control bladder-chips and n=4 infected bladder-chips. Data obtained
568 from n=95 and n=116 fields of view, each of which was 206 x 206 μm^2. (**D**) Quantification of
569 the number of neutrophils detected on the epithelial layer, in control and infected bladder-chips.
570 The red bar represents the median value, $p<1E-15$. In many instances in the uninfected control
571 bladder-chips, no neutrophil diapedesis is detected. Data obtained from n=95 and n=130 across
572 206 x 206 μm^2 fields of view. (**E**) A plot of the maximum neutrophil swarm volume on the
573 epithelial layer normalized to the total volume for n=67 and n=118 fields of view on n=3
574 uninfected control and n=3 infected bladder-chips. The red bar represents the median value.
575 $p<1E-15$. (**F**) A plot of neutrophil swarm volume on the epithelial layer over time for n=51 and
576 n=40 fields of view for n=2 technical replicates indicated by squares and circles. For each time
577 profile, the volume is normalized to the maximum volume attained over the timeseries and t=0
578 refers to the timepoint at which neutrophils are introduced into the vascular channel (**G**) Plot of

579 the time to reach the maximum swarm volume in n=154 fields of view across n=4 infected
580 bladder-chips. (**H1-H5, I1-I5**) NET formation by neutrophils on the epithelial layer. The
581 neutrophils are identified by a cytoplasmic dye (CellTracker Deep Red, false coloured in amber)
582 (**H2, I2)** and immunostaining with an anti-myeloperoxidase antibody (**H3,** zooms in **H5**) or an
583 anti-neutrophil elastase antibody (**I3,** zooms in **I5**). Merged images in each case are shown in **H4**
584 and **I4**. UPEC identified via YFP expression is shown in spring green. Nuclear labelling with
585 DAPI is shown in azure. (**H5**) NETs, identified via anti-myeloperoxidase staining or anti-elastase
586 staining are indicated with white arrows in (**H5**) and (**I5**) respectively. (**J1-J4**) Scanning electron
587 micrographs of the epithelial layer of an infected bladder-chip 2 hours after the introduction of
588 neutrophils in the endothelial channel. (**J1**) Neutrophils (amber arrowheads) are visible above a
589 layer of epithelial cells. Thick bundles consisting of many thinner NET structures between
590 neutrophils are indicated by white arrowheads, and examples of individual UPEC bacteria within
591 the NETs are indicated by green arrowheads. A heavily infected epithelial cell with UPEC
592 visible on the epithelial cell (purple arrowhead), and appendages between epithelial cells (cyan
593 arrowheads) are also visible. (**J2)** Micrographs showing thick bundles consisting of many thinner
594 NET structures (white arrowheads) that extend between cells and trap many individual bacteria.
595 Thinner NET fibers (yellow arrowheads) are also visible. (**J3**) Zooms of the regions in **J2**
596 identified by a yellow dashed square. Two bacteria held by a thick bundle composed of many
597 thinner NET fibers are shown. (**J4**) Micrograph highlighting multiple bacteria trapped between
598 NET bundles. p-values in **D** and **E** were calculated using a Mann-Whitney test. Scale bar = 50
599 μm in **B1-B5**, **H1-H5, I1-I5**.

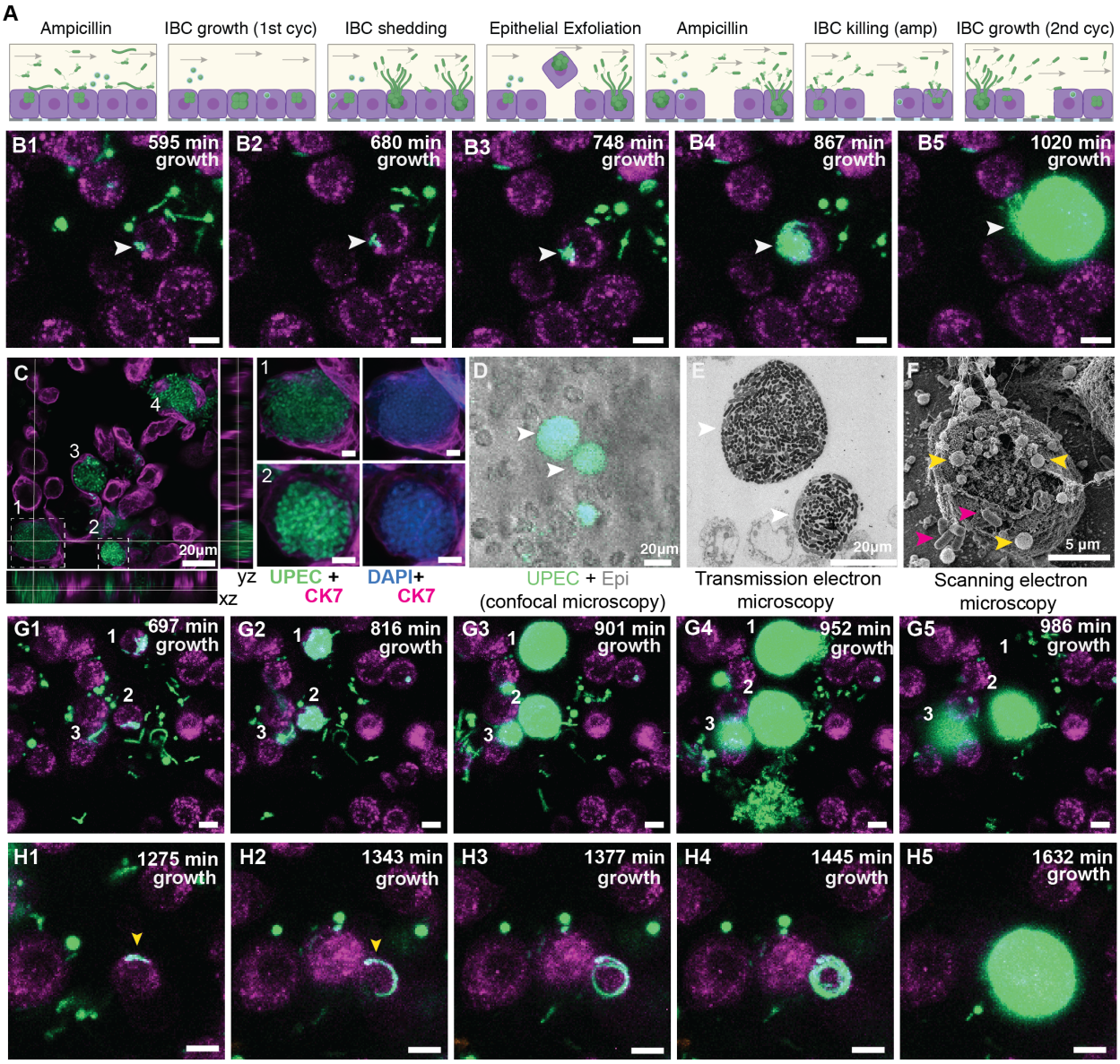

Figure 3: Bladder-chip reveals dynamics of IBC growth, shedding and exfoliation.

(**A**) Schematics of the host-pathogen interactions within IBCs between successive rounds of antibiotic treatment with outcomes including shedding of bacteria and cell exfoliation shown. (**B1-B5**) Timeseries for the growth of an IBC from few bacteria (white arrowhead) after the first round of ampicillin treatment. Bacteria grow to completely fill the cell volume (**B5**). (**C**) Immunofluorescence characterization of two IBCs; the intracellular nature of growth is confirmed with staining with an anti-CK7 antibody. Correlative light (**D**) and transmission

608 electron micrographs (**E**) show two IBCs filled with both rod-shaped and coccoid-shaped
609 bacteria. (**F**) Coccoid-shaped bacteria (yellow arrowheads) and rod-shaped bacteria (magenta
610 arrowheads) are also visible in a scanning electron micrograph of an infected epithelial cell.
611 IBCs on infected bladder-chips shown in **C**-**F** were fixed 13 hours after UPEC infection and 6
612 hours into the first growth cycle. (**G1-G5**) Three examples of IBC growth, labelled 1 – 3 with
613 differing outcomes. Unrestricted bacterial growth is observed within all IBCs. In IBC#1 at
614 timepoint (**G4**) the IBC begins to shed bacteria into the surrounding medium. The cell exfoliates
615 in the time interval between (**G4** and **G5**). In IBC#2, bacterial shedding is visible at (**G4**) and
616 shedding continues until end of the timeseries with a reduction in bacterial volume. In contrast,
617 growth within IBC#3 is slower and neither shedding nor exfoliation occurs within the timeseries.
618 (**H1**-**H5**) Timeseries highlighting an example of filamentous UPEC growth within an IBC. Scale
619 bars, 10 μm in **B1**-**B5**, **G1**-**G5** and **H1**-**H5**.

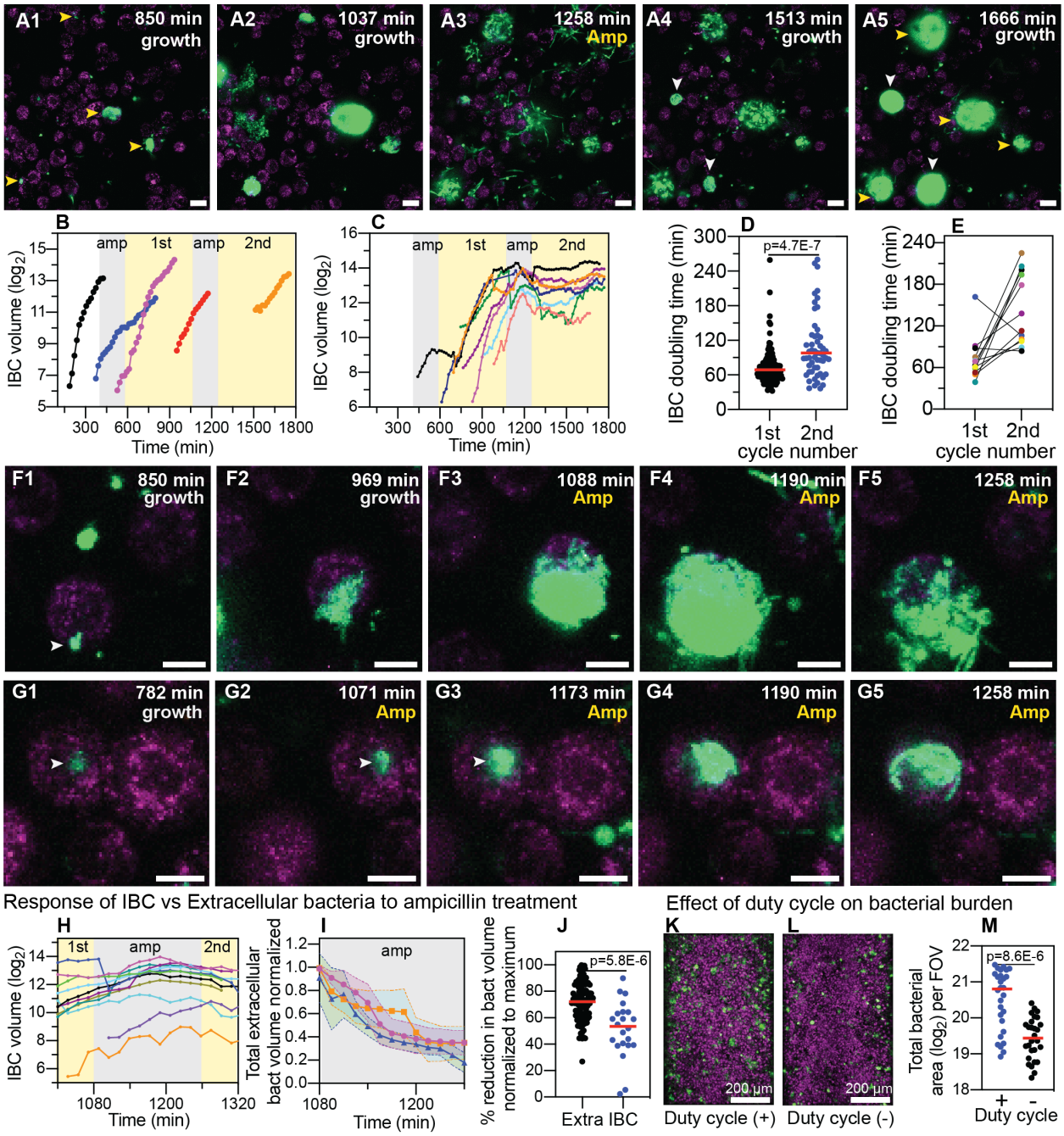

Figure 4: IBCs offer a semi-protective niche that delays clearance of bacteria by antibiotics. (**A1-A5**) Bacteria persist and grow in IBCs despite antibiotic treatment. Snapshots show the growth of four IBCs with variable growth rates (**A1-A2**). Ampicillin treatment eliminates some but not all of the bacteria within each IBC (**A3**). Growth resumes at all sites in (**A4**, **A5**), formation of new IBCs in the second growth cycle is indicated by white arrowheads. (**B**) Plots of logarithm of bacterial volume within five separate IBCs demonstrates exponential bacterial

627 growth. IBCs are seeded dynamically; growth can occur either in the first or second growth
628 cycle, or prior to the administration of antibiotic, or in few cases continues in the presence of the
629 antibiotic. (**C**) Plots of the logarithm of bacterial volume vs. time for n=8 IBCs tracked across
630 two growth phases with an intermediate period of ampicillin treatment. In the growth phases,
631 growth is exponential and bacterial volume continues to increase for up to ca. 120 minutes after
632 administration of antibiotic before declining due to loss of bacteria. In each case, growth resumes
633 after the antibiotic is removed. (**D**) Scatter plots of the doubling time of bacterial volume in IBCs
634 as measured in the first growth cycle (n=102) and the second growth cycle (n=59). Growth in the
635 second cycle is significantly slower (p=4.7E-7), red line represents the median value. (**E**)
636 Doubling time of bacterial volume in IBCs in the first and second growth cycle for some of the
637 IBCs in (**D**) that survived the antibiotic treatment. In n=16 out of 18 instances, growth is slower
638 in the second growth cycle. (**F1**-**F5**) High resolution time-series that highlights bacterial growth
639 within an IBC prior to (**F1**, **F2**) and after (**F3-F5**) administration of ampicillin. Some bacteria
640 within this IBC are subsequently eliminated (**F5**). (**G1**-**G5**) High resolution time-series that
641 highlights bacterial growth within an IBC prior to (**G1**, **G2**) and after (**G3-G5**) administration of
642 ampicillin. The bacterial volume within this IBC is not diminished by antibiotic treatment (**G5**).
643 (**H**) Plots of logarithm of bacterial volume within n=11 IBCs before, during, and after the second
644 round of antibiotic treatment. (**I**) Plot of the volume of extracellular bacteria upon antibiotic
645 administration from n=103 across 206 x 206 μm^2 field of view from n=3 bladder-chips. The
646 bacterial volumes are normalized to the volume immediately prior to the antibiotic
647 administration. (**J**) Scatter plot of the extracellular bacterial volume (n=105) and bacterial
648 volume within IBCs (n=22) after antibiotic treatment as a fraction of the maximum bacterial
649 volume prior to antibiotic treatment. Red line represents the median value, p=5.8E-6 as

650 calculated by Mann-Whitney test. (**K**, **L**) Representative images from the epithelial face of the
651 infected bladder-chips with or without duty cycle. (**M**) Scatter plots of the logarithm of the total
652 bacterial area across n=14 from infected bladder-chips with (n=2) and without (n=2) duty cycle,
653 p= 8.6E-6. Infected bladder-chips shown in **K**, **L** were fixed 13 hours after UPEC infection and 6
654 hours into the first growth cycle. p-values calculated using a Mann-Whitney test. Scale bars, 10
655 μm in panels **A1**-**A5**, **F1**-**F5**, and **G1**-**G5**.
656

Cell type	Cell density/$10^4 \mu m^2$
Epithelial	31.7 ± 5.1
Endothelial	4.0 ± 0.6

Table 1.
Characterization of epithelial and endothelial cell densities from a total of n=18 fields of view in both the epithelial and endothelial layers from n=2 bladder-chips.

Acknowledgements

V.V.T gratefully acknowledges support by a Human Frontier Science Program (HFSP) Long-Term Fellowship (LT000231/2016-L) and a European Molecular Biology Organization (EMBO) Long-Term Fellowship (921-2015). This research was supported by a grant awarded to J.D.M by the Swiss National Science Foundation (SNSF) (Project Funding, 310030B_176397) and the National Centre of Competence in Research AntiResist (51NF40_180541), funded by the SNSF. The authors thank the entire team of EPFL Bioimaging & Optics Core Facility for their assistance in confocal live cell imaging and post analysis in Bitplane Imaris. The authors also acknowledge Marie Croisier at the EPFL Biological Electron Microscopy Facility for help in optimizing the protocol for TEM of infected bladder-chip. The authors thank and credit BioRender.com for the illustrations and schematics used in this manuscript.

673 **Materials and Methods**

Reagent or resource	Designation	Source or reference	Identifiers	Additional information
strain, strain background	Uropathogenic Escherichia coli (UPEC) strain CFT073	PMID: 2182540	NCBI: txid199310	originally isolated from a pyelonephritis patient and provided by Prof. H.L.T. Mobley, University of Michigan, USA
plasmid	pZA32-YFP	PMID: 9092630		(Lutz and Bujard, 1997)
strain, strain background	CFT073-pZA32-YFP	this paper		this study
cell line (human)	HTB-9™ bladder epithelial cells	ATCC	Cat#:5637	
cell line (human)	HMVEC-Bd – Human Bladder Microvascular Endothelial Cells	Lonza	Cat#:7016	
other	RPMI-1640 medium	ATCC	Cat#:30-2001	
other	Gibco™ RPMI 1640 Medium, no phenol red	Thermofisher	Cat#:11835063	
other	Gibco™ Fetal Bovine Serum, Premium Plus	Thermofisher	Cat#: A4766801	
other	EGM™-2 MV Microvascular Endothelial Cell Growth Medium-2 BulletKit™	Lonza	Cat#:CC-3202	
other	EBM-PRF Endothelial Medium Phenol-red free, 500 ML	Lonza	Cat#:CC-3129	
other	EGM™-2 Endothelial SingleQuots™ Kit	Lonza	Cat#:CC-4176	
other	Gibco™ Antibiotic-Antimycotic (100X)	Thermofisher	Cat#:15240062	
other	Gibco™ Trypsin-EDTA (0.05%), phenol red	Thermofisher	Cat#:25300054	
drug	Chloramphenicol	Sigma-Aldrich	Cat#:C1919-25G	34 mg/ml in ethanol (stored at -20 ºC)
drug	Ampicillin	Sigma-Aldrich	Cat#: A9518-5G	50 mg/ml in ddH_2O (stored at -80 ºC)
other	pooled human female urine	Golden West Diagnostics	Cat#: OH2010-pH	
other	Phosphate Buffered Saline	Thermofisher	Cat#: 10010056	
other	Gibco™ HEPES	Thermofisher	Cat#: F2006	
other	Invitrogen™ DAPI	Thermofisher	Cat#: D1306	5 mg/ml in DMSO
other	LB (Luria broth base, Miller's modified)	Sigma-Aldrich	Cat#: L1900-1KG	

other	Organ-chips (Standard Research Kit - 24 per Pack)	Emulate	RE1000001024	Emulate, Inc. 27 Drydock Ave, 5th Floor Boston, MA 02210
other	CellMask™ Orange Plasma membrane Stain	Thermofisher	Cat#: C10045	used at 1µM in respective cell medium
other	HCS CellMask™ Deep Red Stain	Thermofisher	Cat#: H32721	used at 2µM in PBS
other	CellTracker™ Deep Red Dye	Thermofisher	Cat#: C34565	used at 1µM in respective cell medium
other	Elveflow® OB1 Pressure Controller OB1 Base MkIII+	Elveflow	Cat#: OB1MKIII+-MIX-	connected to 6bar compressed air channel
other	Elveflow® OB1 Pressure Controller OB1 MkIII Channel-900/1000	Elveflow	Cat#: OB1-Dual-	connected to Elveflow® OB1 Pressure Controller OB1 Base MkIII+
other	Diaphragm moist gas vacuum pump	KNF Neuberger	Cat#:LABOPORT® UN 820.3 FT.40P	connected to Elveflow® OB1 Pressure Controller OB1 MkIII Channel-900/1000
antibody	Anti-EpCAM	abcam	Cat#: ab71916	used at 1:100 dilution in 1% BSA, conjugated with Donkey anti-Rabbit secondary antibody, Alexa Fluor 647 (2µg/ml) and Alexa Fluor 568 (2µg/ml) in 1%BSA
antibody	Anti-PECAM1 or Anti-CD31	abcam	Cat#: ab24590	used at 1:100 dilution in 1% BSA, conjugated with Donkey anti-Mouse secondary antibody, Alexa Fluor 647 (2µg/ml) and Goat anti-Mouse Alexa Fluor 488 (2µg/ml) in 1%BSA
antibody	Anti-CK7	abcam	Cat#: ab209599	used at 1:100 dilution in 1% BSA
antibody	Anti-CK8	abcam	Cat#: ab192468	used at 1:100 dilution in 1% BSA
other	Alexa Fluor™ 555 Phalloidin	Thermofisher	Cat#: A34055	used at 1µM concentration in PBS

antibody	Anti-VE-Cadherin	abcam	Cat#: ab33168	used at 1:100 dilution in 1% BSA, conjugated with Donkey anti-Rabbit secondary antibody, Alexa Fluor 647 (2µg/ml) and Alexa Fluor 488 (2µg/ml) in 1%BSA
antibody	Anti-Uroplakin3a	Santa Cruz	Cat#: sc-166808	used at 1:100 dilution in 1% BSA, conjugated with Donkey anti-Mouse secondary antibody, Alexa Fluor 647 (2µg/ml) in 1%BSA
antibody	Anti-CK1	Thermofisher	Cat#: MA1-06312	used at 1:100 dilution in 1% BSA, conjugated with Donkey anti-Mouse secondary antibody, Alexa Fluor 647 (2µg/ml) in 1%BSA
antibody	Anti-E-Cadherin	Thermofisher	Cat#: MA5-14408	used at 1:100 dilution in 1% BSA, conjugated with Donkey anti-Mouse secondary antibody, Alexa Fluor 647 (2µg/ml) in 1%BSA
antibody	Anti-ZO-1	abcam	Cat#: ab216880	used at 1:100 dilution in 1% BSA, conjugated with Donkey anti-Rabbit secondary antibody, Alexa Fluor 647 (2µg/ml) in 1%BSA
antibody	Anti-myeloperoxidase	abcam	Cat#: ab9535	used at 1:100 dilution in 1% BSA, conjugated with Donkey anti-Rabbit secondary antibody, Alexa Fluor 568 (2µg/ml) in 1%BSA
antibody	Anti-neutrophil elastase	abcam	Cat#: ab68672	used at 1:100 dilution in 1% BSA, conjugated with Donkey anti-Rabbit secondary antibody, Alexa

				Fluor 568 (2µg/ml) in 1%BSA
antibody	Anti-CD15	abcam	Cat#: ab665	used at 1:100 dilution in 1% BSA, conjugated with Donkey anti-Mouse secondary antibody, Alexa Fluor 568 (2µg/ml) in 1%BSA
antibody	Donkey anti-Mouse IgG (H+L) Highly Cross-Adsorbed Secondary Antibody, Alexa Fluor 647	Thermofisher	Cat#: A-31571	2 mg/ml
antibody	Donkey anti-Rabbit IgG (H+L) Highly Cross-Adsorbed Secondary Antibody, Alexa Fluor 647	Thermofisher	Cat#: A-31573	2 mg/ml
antibody	Goat anti-Mouse IgG (H+L) Highly Cross-Adsorbed Secondary Antibody, Alexa Fluor 488	Thermofisher	Cat#: A-11029	2 mg/ml
antibody	Donkey anti-Rabbit IgG (H+L) Highly Cross-Adsorbed Secondary Antibody, Alexa Fluor 568	Thermofisher	Cat#: A10042	2 mg/ml
antibody	Donkey anti-Mouse IgG (H+L) Highly Cross-Adsorbed Secondary Antibody, Alexa Fluor 568	Thermofisher	Cat#: A10037	2 mg/ml
peptide, recombinant protein	Fibronectin from human plasma	Sigma-Aldrich	Cat#: F1056	500 µg/ml in ddH_2O
peptide, recombinant protein	Native Collagen, Bovine dermis	AteloCell	Cat#: IAC-50	5 mg/ml
peptide, recombinant protein	Human IL-1α, research grade	Miltenyi Biotec	Cat#:130-093-894	1 µg/ml
peptide, recombinant protein	Human IL-1β, research grade	Miltenyi Biotec	Cat#:130-093-895	1 µg/ml
peptide, recombinant protein	Human IL-6, research grade	Miltenyi Biotec	Cat#:130-093-929	1 µg/ml
peptide, recombinant protein	Human IL-8, research grade	Miltenyi Biotec	Cat#:130-122-354	1 µg/ml
commercial assay or kit	MACSxpress® Whole Blood Neutrophil Isolation Kit, human	Miltenyi Biotec	Cat#:130-104-434	
software, algorithm	Imaris 9.5.1	Bitplane		

other	Gas chamber for stages with k-frame insert (160x110mm) - magnetic model with sliding lid.	okolab	Cat#: H201-K-FRAME	
other	Custom holder for 24mm x 60mm coverslip	okolab	Cat#:1x24by60-M	
other	µ-Slide 8 Well	ibidi	Cat#:80826	
other	Masterflex PharMed tubing, 0.89mm ID, 100 ft	Cole-Palmer	Cat#:GZ-95709-26	
other	Masterflex® Transfer Tubing, Tygon® 0.76mm ID	Cole-Palmer	Cat#:GZ-06419-03	
other	1.30 x 0.75 x 10 mm metallic tubes	Unimed	Cat#:9084 / 200.010-A	
other	1.00/0.75 x 20mm metallic tubes	Unimed	Cat#:200.010-A	
other	Aladdin programmable pump	WPI	Cat#: PUMP-NE-1000	

674

675 **Cell culture of human bladder epithelial and bladder endothelial cells**

676 The HTB9 human bladder epithelial carcinoma cell line (procured from ATCC, 5637) was
677 cultured in RPMI 1640 medium supplemented with 10% Fetal Bovine Serum (FBS) as
678 recommended by the supplier. Human Bladder Microvascular Endothelial cells (HMVEC-Bd)
679 (procured from Lonza, CC-7016) were cultured in Lonza EGM-2 MV BulletKit medium. Both
680 the epithelial and endothelial cells were generally cultured in their respective medium
681 supplemented with 1X Antibiotic-Antimycotic. Epithelial cells were passaged by detachment
682 with 0.05% Trypsin at 37°C for 3-5 minutes followed by neutralization of trypsin with RPMI
683 1640 medium/10% FBS. Bladder endothelial cells were passaged and split as recommended by
684 the supplier. The cells used in all the experiments were at ten passages or fewer. The cell lines
685 were tested routinely for mycoplasma contamination during passaging.

686 **UPEC culture for infection of bladder epithelial cells in the bladder-chip**

687 Uropathogenic *Escherichia coli* (UPEC) strain CFT073 was originally isolated from a
688 pyelonephritis patient (Mobley et al., 1990) and provided by Prof. H.L.T. Mobley, University of
689 Michigan, USA. A derivative strain expressing yellow fluorescent protein (YFP) was generated

690 by electroporation of CFT073 with the episomal plasmid pZA32-YFP (Lutz and Bujard, 1997),
691 as described earlier (Dhar et al., 2015). To induce expression of type 1 pili, UPEC was grown in
692 LB media containing 25 μg/ml chloramphenicol under non-shaking conditions at 37 ^{0}C for 2
693 days prior to the experiment, to achieve a stationary phase culture (OD_{600}=1.5 and corresponding
694 to a concentration of 1.5 x 10^{9} bacteria/ml). The bacteria were diluted 10-fold to a final
695 concentration of 1.5 x 10^{8} cells/ml) and resuspended in a solution of pooled human female urine
696 (procured from Golden West Diagnostics Catalogue OH2010-pH) diluted 10-fold in Phosphate
697 Buffered Saline.
698
699 **Recapitulation of human bladder physiology in human bladder-on-a-chip device**
700 Bladder-chip devices made of polydimethylsiloxane (PDMS) were purchased from Emulate
701 (Boston, USA). The dimensions of the microfluidic device were as follows: width of the
702 channels- 1000 μm, height of the upper channel- 1000 μm, lower channel – 250 μm). For
703 extracellular matrix (ECM) coating, a coating solution consisting of the ER-1 compound
704 (Emulate) dissolved in ER-2 solution at 0.5 mg/ml (Emulate) was introduced in both apical and
705 vascular channels and the chips were subsequently activated by exposing the bladder-chip for 20
706 minutes under UV light. The channels were then rinsed with fresh coating solution and the
707 protocol was repeated once. The channels of the bladder-chip were then washed thoroughly with
708 PBS before incubation with an ECM solution of 150 μg/ml bovine collagen type I and 30 μg/ml
709 fibronectin from human plasma in PBS buffered with 15 mM HEPES solution for 1-2 hours at
710 37°C as described previously (Thacker et al., 2020b). If not used directly, coated chips were
711 stored at 4°C and pre-activated before use by incubation for 30 minutes with the same ECM
712 solution at 37°C. Three days before the day of the experiment, HMVEC-Bd cells were seeded

713 into lower channel of the inverted bladder-chip device at 0.5 million cells/ml. Two days before
714 the experiment, HTB9 cells were seeded into upper channel at 5 million cells/ml. Prior to the
715 infection experiment, bladder endothelial and bladder epithelial cells were cultured in their
716 respective medium supplemented with the 1X Antibiotic-Antimycotic solution. The antibiotics
717 were removed prior to the experiment.
718
719 **Characterization and immunostaining of human bladder epithelial and human bladder**
720 **epithelial cells in ibidi wells and human bladder-chip**
721 Human bladder epithelial and bladder endothelial cells were cultured inside ibidi μ–Slide 8 wells
722 for one day. The cells were subsequently fixed with 4% paraformaldehyde (PFA) for 1 hour at
723 room temperature. Fixed cells were then washed three times with 200 μl of PBS to remove
724 residues of PFA, permeabilized with 0.15 % Triton X-100 for 15 minutes; washed three times
725 with 200 μl of PBS to remove residues of detergent and then incubated in a blocking solution of
726 1% BSA in PBS for 1 hour. The cells were then incubated with primary antibodies (anti-
727 EpCAM, anti-PECAM-1, anti-CK7, anti-CK8, anti-VE-Cadherin, anti-Uroplakin3a, anti-CK1,
728 anti-E-Cadherin, anti-ZO-1, anti-myeloperoxidase, anti-neutrophil elastase, anti-CD15) at a
729 dilution of 1:100 in an antibody incubation buffer comprising 1% BSA and 0.01% Triton-100 in
730 PBS. The ibidi 8-wells were subsequently washed three times with PBS for 10 minutes each.
731 Incubation with secondary antibody (Donkey anti-Mouse Alexa Fluor 647, Donkey anti-Mouse
732 Alexa Fluor 568, Goat anti-Mouse Alexa Fluor 488, Donkey anti-Rabbit Alexa Fluor 647,
733 Donkey anti-Rabbit Alexa Fluor 568, Donkey anti-Rabbit Alexa Fluor 488) at a concentration of
734 2 μg/ml in antibody incubation buffer was subsequently performed for 1 hour at room
735 temperature. Excess antibody was removed by washing three times with PBS for 10 minutes

736 each. Cell nuclei were stained with DAPI (5 µg/ml) for 30 minutes. Ibidi 8-wells were washed
737 three times to remove unbound DAPI. Cells were covered with appropriate volume of PBS until
738 imaging. Cells were imaged with 63X oil objective on Leica SP8 confocal microscope. Images
739 were deconvolved using SVI Huygens (Quality, 0.05; Iterations, 40).
740
741 For characterization of the cell types on-chip, bladder-chips with co-culture of bladder epithelial
742 and bladder endothelial cells were kept under pooled diluted urine and EBM2 medium using
743 P200 pipette tips for 2 days prior to PFA fixation. The cells in the bladder-chip were then
744 immunostained following the protocol described above. Images were acquired with Leica HC
745 FLUOTAR 25X (NA 0.95) multi-immersion objective on Leica SP8 confocal microscope.
746
747 **Characterization of strain-pressure curve in the bladder-chip model**
748 Elveflow OB1 MK3 – Microfluidic flow control system was used to control the negative
749 pressure applied to the human bladder-chip. The control system was connected to the
750 compressed air line (6 bar) for the positive pressure and diaphragm vacuum pump for the
751 negative pressure. A negative pressure (0 to -900 mbar) with a step function of -100mbar was
752 subsequently applied to the vacuum channels in the bladder-chip using a Pressure Controller
753 (Elveflow OB1 pressure controller). For these experiments, both bladder epithelial and
754 endothelial cells were seeded on the respective sides in the devices. This experiment was
755 performed with the chip maintained on the stage of the microscope and a brightfield image was
756 acquired at each step increase of -100mbar, on Leica SP8 confocal microscope. The PDMS inter-
757 pore-to-pore distance was measured for 14 pore-to-pore combinations at each input of negative
758 pressure. Linear fitting was performed using GraphPad Prism (version 9).

759

760 **Mimicking bladder filling and voiding cycle in human bladder-chip**

761 The stretching of the human bladder-chip was done using the Elveflow OB1 MK3 – Microfluidic
762 flow control system connected to the compressed air line (6 bar) for the positive pressure and
763 diaphragm vacuum pump for the negative pressure. Human bladder-chip in the relaxed (*voided*
764 *bladder*) state was slowly perturbed with a linear ramp function to reach a stretched (*filled*
765 *bladder*) state over a period of 2 hours. This period corresponded to the *filling bladder* state in
766 Figure 1D. Bladder-chip was kept under stretched (*filled bladder*) state over the subsequent 2
767 hours. Micturition or urination was recapitulated by rapidly reducing the applied strain on the
768 bladder-chip from the stretched (*filled bladder*) state to relaxed (*voided bladder*) state over a
769 period of 2 minutes. Subsequently, the bladder-chip was maintained with no negative pressure
770 applied in the vacuum channel under relaxed (*voided bladder*) state from (4:02 hours to 6 hours).
771 This 6-hour bladder filling and voiding cycle was repeated continuously for the rest of the
772 experiment.

773 **Experimental setup and imaging parameters for time lapse imaging for UPEC infection in**
774 **the human bladder-chip devices**

775 The medium perfusion inside the bladder-chip device was achieved with the Aladdin syringe
776 pumps. The syringes with respective media were connected to the bladder-chip via gas
777 impermeable PharMed® tubing (inner diameter =0.89 mm, Cole palmer GZ-95809-26) along
778 with longer transparent Tygon tubings (internal diameter of 0.76mm, Masterflex transfer tubing,
779 Cole palmer). The Harmed® tubing was connected to the inlet and outlet of the bladder-chip
780 with 1.30 x 0.75 x 10 mm metallic tubes (Unimed) and transparent tubing with 1.00/0.75 x
781 20mm metallic tubes (Unimed). The bladder-chip connected to external sources of flow was then

782 mounted onto a 24 x 60 mm No. 1 glass coverslip for microscopy imaging. When required for
783 stretching experiments, tubing was also connected to the stretching channels on either side of the
784 main channel. The connected device was subsequently assembled inside a temperature-
785 controlled microscope environmental chamber at 37ºC supplemented with 5% CO_2 (OKO labs).
786 Time-lapse imaging was conducted using a Leica HC FLUOTAR 25X (NA 0.95) multi-
787 immersion objective within custom made environmental chamber set at 37ºC for infusion with
788 syringe pumps. Water was pumped to the ring around the water objective at 9 Hz with pumping
789 duration of 9 seconds and pumping interval 30 minutes, controlled by SRS software (HRZ=9,
790 VPP=95). The autofocus mode (best focus, steps =9, range = 30 µm) was used to maintain the
791 optical focus on the apical side of the PDMS membrane. The experiments were monitored
792 frequently to ensure that the optical focus was maintained, and the experiment was halted and
793 restarted if the focus was lost.
794 To enable rapid 3-D imaging across multiple spatial locations on-chip, we utilized the capability
795 of the white light laser on the Leica SP8 confocal microscope to image at multiple wavelengths
796 simultaneously. The excitation wavelengths were grouped into two sequences to minimize the
797 spectral overlap. In the first sequence, laser emission at 555 nm was used to excite the Calmest
798 Orange stain in the bladder epithelial cells. In the second laser excitation sequence, laser
799 emission at 500 nm and 630 nm were used to excite the YFP within the bacteria and the
800 cytoplasmic CellTracker™ Deep Red in the human neutrophils. Images were acquired with a
801 scan speed of 400-700 Hz and a zoom factor of 2.25 (206.67 µm x 206.67 µm) resulting in an
802 XY resolution of 450 nm depending on the number of pixels acquired per field of view. Z-stacks
803 were acquired with 1 µm step sizes. Time lapse images were acquired with interval duration of

804 ca. 15-17 minutes, in a subset of experiments this was further reduced to 7.5 minutes by imaging
805 with the second sequence only at a z-step size of 2 µm.
806
807 **Time lapse imaging for UPEC infections in the human bladder-chip devices**
808 Pre-infection stage
809 The time-course of the entire experimental protocol is shown in a schematic in Figure 1. The
810 bladder-chip device was perfused with diluted urine in the apical channel and EBM Endothelium
811 phenol-red free medium supplemented with EGM-2 endothelial SingleQuots kit in the vascular
812 channel. Prior to the commencement of infection, the chip was maintained at homeostasis and
813 the epithelial cells were imaged for a period of two hours.
814
815 Infection stage
816 Stationary phase UPEC in diluted pooled urine at a concentration of 150 million cells/ml were
817 flowed through the apical channel of the device at 1200 µl/hour for 1.5 hours. During this period,
818 EBM2 media was flowed through the endothelial channel at 600 µl/hour.
819
820 Bacterial washout and neutrophil introduction stage
821 Next, the syringe connected to the apical channel was replaced with a fresh syringe containing
822 pooled diluted urine, this solution was then flowed in the apical channel over the epithelial layer
823 of the chip at a flow rate of 600 µl/hour over the next 3 hours. This allowed for the continuous
824 removal of extracellular planktonic bacteria in the apical channel. At the same time, human
825 neutrophils were introduced into the endothelial channel of the bladder-chip via flow. A solution
826 of human neutrophils at a density of 2 million cells/ml isolated via negative selection was flowed

827 through the vascular channel for 2 hours in EBM2 medium with at higher shear stress of η=1.0
828 dyne/cm^2 to enhance neutrophil attachment to endothelial cells.
829
830 Neutrophil diapedesis stage
831 Diapedesis of human neutrophils to epithelial side and subsequent interactions of neutrophils
832 with UPEC was observed for the subsequent 3 hours since introduction of neutrophils into the
833 vasculature side of the chip. During this period, the flow rate in the apical and vascular channels
834 were maintained at 600 µl/hour and 3000 µl/hour, respectively. During this period, in a subset of
835 experiments, only the channels that were part of the second laser scanning sequence were
836 imaged. Images of the CellTracker Orange dye for epithelial cell identification were not acquired
837 (first laser scanning sequence). This enabled a number of fields of view to be captured with an
838 enhanced temporal resolution and a frame rate of up to 7.5 minutes. For experiments studying
839 the formation of NETs, the experiment was halted at this stage and the infected chips were fixed,
840 permeabilized, blocked, and immunostained with anti-myeloperoxidase (abcam) or anti-
841 neutrophil elastase (abcam) antibodies using the procedure described earlier. For all other
842 experiments, live imaging continued to the subsequent antibiotic treatment phase,
843 Immunofluorescence for anti-myeloperoxidase and anti-neutrophil elastase was done as the
844 procedure described previously.
845
846 Antibiotic treatment and growth cycles
847 Thereafter, syringes connected to both apical and vascular channels were changed and ampicillin
848 at 250 µg/ml (used at ~40-fold over the minimum inhibitory concentration (MIC) of ampicillin
849 against UPEC grown in EBM2 medium) was introduced in the diluted urine and the EBM2

850 media perfused into the apical and vascular channels, respectively, for 3 hours at a flow rate of
851 600 µl/hour. This was the first ampicillin treatment cycle; whose purpose was to eliminate
852 extracellular bacteria in the apical channel and allow intracellular bacterial colonies (IBCs) to be
853 identified. The medium was subsequently switched with antibiotic-free medium for next 8 hours
854 to allow for IBC growth within epithelial cells. During this period, the flow within the apical
855 channel was maintained, to remove bacteria that grew extracellularly either because they
856 survived the antibiotic treatment or that were released from infected epithelial cells. The
857 ampicillin and growth cycle were then repeated, to allow the assessment of the response of
858 bacteria within IBCs to antibiotic treatment as well as characterize the subsequent regrowth.
859

860 **Image analysis of confocal live-cell images**

861 Image analysis was performed with Bitplane Imaris 9.5.1. The time-lapse imaging stack included
862 five channels: uroepithelial cells (epithelial channel), transmitted light (bright field channel),
863 UPEC (bacterial channel), neutrophils (neutrophil channel), and transmitted light (bright field
864 channel). Neutrophils were identified via the spot detection algorithm in Imaris used on the
865 images from the neutrophil channel with the following parameters (Size, 8 µm; Quality, 4 to 8).
866 Swarms of neutrophils generate dense aggregates that are ill-suited to quantification with the
867 spot detection algorithm. To quantify the size of the swarms, we therefore segmented images in
868 the neutrophil channel to generate surfaces via the automatic segmentation tool in Imaris with the
869 following parameters (Threshold, 10; Smooth Surfaces Detail, 0.5 or 1.0 µm). Unfortunately, the
870 time resolution was insufficient to track individual neutrophils over time particularly since
871 neutrophils formed small clumps and rapidly changed their cell shapes.

872 For UPEC volume inside IBCs, necessary 3D volume was cropped in Imaris to ease image
873 analysis. Total bacterial volume inside IBC was detected by creating the surface (Threshold, 15;
874 Smooth Surfaces Detail, 0.5 or 1 µm) on UPEC channel.
875 In cases of measuring extracellular UPEC growth, surface was generated (Threshold, 15; Smooth
876 Surfaces Detail, 0.5 or 1 µm) on UPEC channel to calculate total extracellular volume in the
877 field of view.
878
879 **Isolation and Labelling of human neutrophils from fresh human blood**
880 Primary human neutrophils were isolated via negative depletion method from human blood with
881 MACSxpress® Whole Blood Neutrophil Isolation Kit (Miltenyi Biotec), following the
882 manufacturer's instructions. Isolation was performed without the use of a density-based
883 centrifugation method. Isolated human neutrophils were then incubated with a 1µM solution
884 CellTracker™ Deep Red in a serum free RPMI phenol red free medium for 30 minutes in a cell
885 culture incubator maintained at 37 C and 5% CO_2. Labelled human neutrophils were then
886 washed with 10ml of 20% FBS in RPMI phenol red free medium twice to remove the unbound
887 dye. The human neutrophils were suspended in Lonza EBM2 medium at a cell density of 1
888 million cells/ml. In some instances, labelled human neutrophils were passed through a filter with
889 40 µm pores to remove neutrophil clusters that may have formed during the isolation process.
890
891 **Scanning electron microscopy of human bladder-chip**
892 UPEC within infected human bladder-chips were allowed to proliferate for 6 hours (14 hours
893 from start of UPEC infection) until the end of the first IBC growth cycle. After 6 hours, human
894 bladder-chip was fixed at room temperature for 1 hour with a mix of 1% glutaraldehyde and 2%

895 paraformaldehyde in 0.1 M phosphate buffer (pH 7.4). The fixed bladder-chip was kept in the
896 fixative overnight (at 4°C). Post overnight fixation, human bladder-chip was cut open from the
897 apical channel side. A scalpel was used to cut approximately in the middle of the apical channel
898 side (height=1mm) to expose the bladder epithelial cells. The fixed chip was further fixed for 30
899 minutes in 1% osmium tetroxide in 0.1 M cacodylate buffer followed by washing with the
900 distilled water. Next, the bladder-chip was dehydrated in a graded alcohol series and dried by
901 passing them through the supercritical point of carbon dioxide (CPD300, Leica Microsystems).
902 Finally, the bladder-chip was attached to an adhesive conductive surface followed by coating
903 with a 3 – 4 nm thick layer of gold palladium metal (Quorum Q Plus, Quorum Technologies).
904 Images of the cells were captured using a field emission scanning electron microscope (Merlin,
905 Zeiss NTS).
906 Uninfected human bladder-chip controls were fixed at the same time point (14 hours from start
907 of the experiment). For the case of NETs formed on epithelial layer, an uninfected human
908 bladder-chip was fixed 2 hours after the introduction of neutrophils into the vascular channel of
909 the chip.
910
911 **Preparation for transmission electron microscopy (TEM)**
912 UPEC within infected human bladder-chips were allowed to proliferate for 6 hours (14 hours
913 from start of UPEC infection) during the first IBC growth cycle. After 6 hours, human bladder-
914 chip was fixed at room temperature for 1 hour with a mix of 1% glutaraldehyde and 2%
915 paraformaldehyde in 0.1 M phosphate buffer (pH 7.4). The fixed bladder-chip was kept in the
916 fixative overnight (at 4°C). Post overnight fixation, human bladder-chip was cut open from the
917 apical channel side. A scalpel was used to cut approximately in the middle of the apical channel

918 side (height-1mm) to expose the bladder epithelial cells. The bladder-chip was then washed in
919 cacodylate buffer (0.1M, pH 7.4), postfixed for 40 minutes in 1.0 % osmium tetroxide with 1.5%
920 potassium ferrocyanide, and then fixed again with 1.0% osmium tetroxide alone. The bladder-
921 chip was finally stained for 30 minutes in 1% uranyl acetate in water before being dehydrated
922 through increasing concentrations of alcohol and then embedded in Durcupan ACM (Fluka,
923 Switzerland) resin. The bladder-chip was then placed in Petri dishes so that approximately 1 mm
924 of resin remained above the cells, and the dish than left in an oven at 65°C for 24 hours. Regions
925 on interest, and corresponding to structures imaged with light microscopy were trimmed from the
926 rest of the device, once the resin had hardened, and thin, 50 nm-thick sections were cut with a
927 diamond knife, and collected onto single-slot copper grids with a pioloform support film. These
928 were contrasted with lead citrate and uranyl acetate, and images taken with a transmission
929 electron microscope at 80 kV (Tecnai Spirit, FEI Company with Eagle CCD camera).
930

931 **Data availability statement**
932 The datasets generated during and analyzed during the current study are available from the
933 corresponding authors on reasonable request and will be uploaded to Zenodo prior to publication.
934

935
936 **Bibliography**
937

938 Abraham, S.N., and Miao, Y. (2015). The nature of immune responses to urinary tract infections.
939 Nat Rev Immunol *15*, 655–663.

940 Agace, W.W., Hedges, S.R., Ceska, M., and Svanborg, C. (1993). Interleukin-8 and the
941 neutrophil response to mucosal gram-negative infection. J Clin Invest *92*, 780–785.

942 Agace, W.W., Patarroyo, M., Svensson, M., Carlemalm, E., and Svanborg, C. (1995).
943 Escherichia coli induces transuroepithelial neutrophil migration by an intercellular adhesion
944 molecule-1-dependent mechanism. Infect Immun *63*, 4054–4062.

945 Alon, R., Hammer, D.A., and Springer, T.A. (1995). Lifetime of the P-selectin-carbohydrate
946 bond and its response to tensile force in hydrodynamic flow. Nature *374*, 539–542.

947 Andersen, T.E., Khandige, S., Madelung, M., Brewer, J., Kolmos, H.J., and Møller-Jensen, J.
948 (2012). Escherichia coli uropathogenesis in vitro: invasion, cellular escape, and secondary
949 infection analyzed in a human bladder cell infection model. Infect Immun *80*, 1858–1867.

950 Anderson, G.G., Palermo, J.J., Schilling, J.D., Roth, R., Heuser, J., and Hultgren, S.J. (2003).
951 Intracellular Bacterial Biofilm-Like Pods in Urinary Tract Infections. Science *301*, 105–107.

952 Apodaca, G. (2004). The Uroepithelium: Not Just a Passive Barrier. Traffic *5*, 117–128.

953 Benam, K.H., Villenave, R., Lucchesi, C., Varone, A., Hubeau, C., Lee, H.-H., Alves, S.E.,
954 Salmon, M., Ferrante, T.C., Weaver, J.C., et al. (2016). Small airway-on-a-chip enables analysis
955 of human lung inflammation and drug responses in vitro. Nat Methods *13*, 151–157.

956 Blango, M.G., and Mulvey, M.A. (2010). Persistence of Uropathogenic Escherichia coli in the
957 Face of Multiple Antibiotics ▿. Antimicrob Agents Ch *54*, 1855–1863.

958 Branzk, N., Libode's, A., Hardison, S.E., Wang, Q., Gutierrez, M.G., Brown, G.D., and
959 Papayannopoulos, V. (2014). Neutrophils sense microbe size and selectively release neutrophil
960 extracellular traps in response to large pathogens. Nat Immunol *15*, 1017–1025.

961 Brinkmann, V., Reichard, U., Goosmann, C., Fauler, B., Uhlemann, Y., Weiss, D.S., Weinrauch,
962 Y., and Zychlinsky, A. (2004). Neutrophil Extracellular Traps Kill Bacteria. Science *303*, 1532–
963 1535.

964 Bryskier, A. (2020). Antimicrobial Agents: Antibacterials and Antifungals. pp. 113–162.

965 Cakir, B., Xiang, Y., Tanaka, Y., Kural, M.H., Parent, M., Kang, Y.-J., Chapeton, K., Patterson,
966 B., Yuan, Y., He, C.-S., et al. (2019). Engineering of human brain organoids with a functional
967 vascular-like system. Nat Methods *16*, 1169–1175.

968 Carattino, M.D., Prakasam, H.S., Ruiz, W.G., Clayton, D.R., McGuire, M., Gallo, L.I., and
969 Apodaca, G. (2013). Bladder filling and voiding affect umbrella cell tight junction organization
970 and function. Am J Physiol-Renal *305*, F1158–F1168.

971 Clevers, H. (2016). Modeling Development and Disease with Organoids. Cell *165*, 1586–1597.

972 Dhar, N., Dubée, V., Ballell, L., Cuinet, G., Hugonnet, J.-E., Signorino-Gelo, F., Barros, D.,
973 Arthur, M., and McKinney, J.D. (2015). Rapid Cytolysis of Mycobacterium tuberculosis by
974 Faropenem, an Orally Bioavailable β-Lactam Antibiotic. Antimicrob Agents Ch *59*, 1308–1319.

975 Duncan, M.J., Li, G., Shin, J.-S., Carson, J.L., and Abraham, S.N. (2004). Bacterial Penetration
976 of Bladder Epithelium through Lipid Rafts. J Biol Chem *279*, 18944–18951.

977 Duraiswamy, S., Chee, J.L.Y., Chen, S., Yang, E., Lees, K., and Chen, S.L. (2018). Purification
978 of Intracellular Bacterial Communities during Experimental Urinary Tract Infection Reveals an
979 Abundant and Viable Bacterial Reservoir. Infect Immun *86*, e00740-17.

980 Ermert, D., Urban, C.F., Laube, B., Goosmann, C., Zychlinsky, A., and Brinkmann, V. (2009).
981 Mouse Neutrophil Extracellular Traps in Microbial Infections. J Innate Immun *1*, 181–193.

982 Foxman, B. (2010). The epidemiology of urinary tract infection. Nat Rev Urol *7*, 653–660.

983 Gloeckner, D.C., SACKS, M.S., FRASER, M.O., SOMOGYI, G.T., GROAT, W.C. de, and
984 CHANCELLOR, M.B. (2002). Passive Biaxial Mechanical Properties of the Rat Bladder Wall
985 After Spinal Cord Injury. J Urology *167*, 2247–2252.

986 Grassart, A., Malardé, V., Gobba, S., Sartori-Rupp, A., Kerns, J., Karalis, K., Marteyn, B.,
987 Sansonetti, P., and Sauvonnet, N. (2019). Bioengineered Human Organ-on-Chip Reveals
988 Intestinal Microenvironment and Mechanical Forces Impacting Shigella Infection. Cell Host
989 Microbe *26*, 435-444.e4.

990 Hannan, T.J., Totsika, M., Mansfield, K.J., Moore, K.H., Schembri, M.A., and Hultgren, S.J.
991 (2012). Host–pathogen checkpoints and population bottlenecks in persistent and intracellular
992 uropathogenic Escherichia coli bladder infection. Fems Microbiol Rev *36*, 616–648.

993 Haraoka, M., Hang, L., Frendéus, B., Godaly, G., Burdick, M., Strieter, R., and Svanborg, C.
994 (1999). Neutrophil Recruitment and Resistance to Urinary Tract Infection. J Infect Dis *180*,
995 1220–1229.

996 Hedges, S., Svensson, M., and Svanborg, C. (1992). Interleukin-6 response of epithelial cell lines
997 to bacterial stimulation in vitro. Infect Immun *60*, 1295–1301.

998 Hopke, A., Scherer, A., Kreuzburg, S., Abers, M.S., Zerbe, C.S., Dinauer, M.C., Mansour, M.K.,
999 and Irimia, D. (2020). Neutrophil swarming delays the growth of clusters of pathogenic fungi.
1000 Nat Commun *11*, 2031.

1001 Horsley, H., Dharmasena, D., Malone-Lee, J., and Rohn, J.L. (2018). A urine-dependent human
1002 urothelial organoid offers a potential alternative to rodent models of infection. Sci Rep-Uk *8*,
1003 1238.

1004 Hsieh, M.M., Everhart, J.E., Byrd-Holt, D.D., Tisdale, J.F., and Rodgers, G.P. (2007).
1005 Prevalence of Neutropenia in the U.S. Population: Age, Sex, Smoking Status, and Ethnic
1006 Differences. Ann Intern Med *146*, 486.

1007 Huh, D., Matthews, B.D., Mammoto, A., Montoya-Zavala, M., Hsin, H.Y., and Ingber, D.E.
1008 (2010a). Reconstituting Organ-Level Lung Functions on a Chip. Science *328*, 1662–1668.

1009 Huh, D., Matthews, B.D., Mammoto, A., Montoya-Zavala, M., Hsin, H.Y., and Ingber, D.E.
1010 (2010b). Reconstituting Organ-Level Lung Functions on a Chip. Science *328*, 1662–1668.

1011 Hung, C.-S., Dodson, K.W., and Hultgren, S.J. (2009). A murine model of urinary tract
1012 infection. Nat Protoc *4*, 1230–1243.

1013 Hunstad, D.A., and Justice, S.S. (2010). Intracellular Lifestyles and Immune Evasion Strategies
1014 of Uropathogenic Escherichia coli. Annu Rev Microbiol *64*, 203–221.

1015 Iosifidis, G., and Duggin, I.G. (2020). Distinct Morphological Fates of Uropathogenic
1016 Escherichia coli Intracellular Bacterial Communities: Dependency on Urine Composition and
1017 pH. Infect Immun *88*.

1018 Jalili-Firoozinezhad, S., Gazzaniga, F.S., Calamari, E.L., Camacho, D.M., Fadel, C.W., Bein, A.,
1019 Swenor, B., Nestor, B., Cronce, M.J., Tovaglieri, A., et al. (2019). A complex human gut
1020 microbiome cultured in an anaerobic intestine-on-a-chip. Nat Biomed Eng *3*, 520–531.

1021 Jang, K.-J., Mehr, A.P., Hamilton, G.A., McPartlin, L.A., Chung, S., Suh, K.-Y., and Ingber,
1022 D.E. (2013). Human kidney proximal tubule-on-a-chip for drug transport and nephrotoxicity
1023 assessment. Integr Biol *5*, 1119–1129.

1024 Jang, K.-J., Otieno, M.A., Ronxhi, J., Lim, H.-K., Ewart, L., Kodella, K.R., Petropolis, D.B.,
1025 Kulkarni, G., Rubins, J.E., Conegliano, D., et al. (2019). Reproducing human and cross-species
1026 drug toxicities using a Liver-Chip. Sci Transl Med *11*, eaax5516.

1027 Justice, S.S., Hung, C., Theriot, J.A., Fletcher, D.A., Anderson, G.G., Footer, M.J., and Hultgren,
1028 S.J. (2004). Differentiation and developmental pathways of uropathogenic Escherichia coli in
1029 urinary tract pathogenesis. Proc National Acad Sci *101*, 1333–1338.

1030 Kang, Y.B. (Abraham), Rawat, S., Duchemin, N., Bouchard, M., and Noh, M. (2017). Human
1031 Liver Sinusoid on a Chip for Hepatitis B Virus Replication Study. Micromachines-Basel *8*, 27.

1032 Kienle, K., and Lämmermann, T. (2016). Neutrophil swarming: an essential process of the
1033 neutrophil tissue response. Immunol Rev *273*, 76–93.

1034 Kim, H.J., and Ingber, D.E. (2013). Gut-on-a-Chip microenvironment induces human intestinal
1035 cells to undergo villus differentiation. Integr Biol *5*, 1130–1140.

1036 Kim, H.J., Li, H., Collins, J.J., and Ingber, D.E. (2016). Contributions of microbiome and
1037 mechanical deformation to intestinal bacterial overgrowth and inflammation in a human gut-on-
1038 a-chip. Proc National Acad Sci *113*, E7–E15.

1039 Klein, R.D., and Hultgren, S.J. (2020). Urinary tract infections: microbial pathogenesis, host-
1040 pathogen interactions and new treatment strategies. Nat Rev Microbiol *18*, 211–226.

1041 Korkmaz, I., and Rogg, B. (2007). A simple fluid-mechanical model for the prediction of the
1042 stress–strain relation of the male urinary bladder. J Biomech *40*, 663–668.

1043 Kreisel, D., Nava, R.G., Li, W., Zinselmeyer, B.H., Wang, B., Lai, J., Pless, R., Gelman, A.E.,
1044 Krupnick, A.S., and Miller, M.J. (2010). In vivo two-photon imaging reveals monocyte-
1045 dependent neutrophil extravasation during pulmonary inflammation. Proc National Acad Sci
1046 *107*, 18073–18078.

1047 Lämmermann, T., Afonso, P.V., Angermann, B.R., Wang, J.M., Kastenmüller, W., Parent, C.A.,
1048 and Germain, R.N. (2013). Neutrophil swarms require LTB4 and integrins at sites of cell death
1049 in vivo. Nature *498*, 371–375.

1050 Ley, K., Laudanna, C., Cybulsky, M.I., and Nourshargh, S. (2007). Getting to the site of
1051 inflammation: the leukocyte adhesion cascade updated. Nat Rev Immunol *7*, 678–689.

1052 Lutz, R., and Bujard, H. (1997). Independent and Tight Regulation of Transcriptional Units in
1053 Escherichia Coli Via the LacR/O, the TetR/O and AraC/I1-I2 Regulatory Elements. Nucleic
1054 Acids Res *25*, 1203–1210.

1055 Martinez, J.J., Mulvey, M.A., Schilling, J.D., Pinkner, J.S., and Hultgren, S.J. (2000). Type 1
1056 pilus-mediated bacterial invasion of bladder epithelial cells. Embo J *19*, 2803–2812.

1057 Metzler, K.D., Fuchs, T.A., Nauseef, W.M., Reumaux, D., Roesler, J., Schulze, I., Wahn, V.,
1058 Papayannopoulos, V., and Zychlinsky, A. (2011). Myeloperoxidase is required for neutrophil
1059 extracellular trap formation: implications for innate immunity. Blood *117*, 953–959.

1060 Mobley, H.L., Green, D.M., Trifillis, A.L., Johnson, D.E., Chippendale, G.R., Lockatell, C.V.,
1061 Jones, B.D., and Warren, J.W. (1990). Pyelonephritogenic Escherichia coli and killing of
1062 cultured human renal proximal tubular epithelial cells: role of hemolysin in some strains. Infect
1063 Immun *58*, 1281–1289.

1064 Mulvey, M.A., Lopez-Boado, Y.S., Wilson, C.L., Roth, R., Parks, W.C., Heuser, J., and
1065 Hultgren, S.J. (1998). Induction and Evasion of Host Defenses by Type 1-Piliated Uropathogenic
1066 Escherichia coli. Science *282*, 1494–1497.

1067 Mysorekar, I.U., and Hultgren, S.J. (2006). Mechanisms of uropathogenic Escherichia coli
1068 persistence and eradication from the urinary tract. Proc National Acad Sci *103*, 14170–14175.

1069 Nagamatsu, K., Hannan, T.J., Guest, R.L., Kostakioti, M., Hadjifrangiskou, M., Binkley, J.,
1070 Dodson, K., Raivio, T.L., and Hultgren, S.J. (2015). Dysregulation of Escherichia coli α-
1071 hemolysin expression alters the course of acute and persistent urinary tract infection. Proc
1072 National Acad Sci *112*, E871–E880.

1073 Nawroth, J.C., Lucchesi, C., Cheng, D., Shukla, A., Ngyuen, J., Shroff, T., Varone, A., Karalis,
1074 K., Lee, H.-H., Alves, S., et al. (2020). A Microengineered Airway Lung Chip Models Key
1075 Features of Viral-induced Exacerbation of Asthma. Am J Resp Cell Mol *63*, 591–600.

1076 Nourshargh, S., Hordijk, P.L., and Sixt, M. (2010). Breaching multiple barriers: leukocyte
1077 motility through venular walls and the interstitium. Nat Rev Mol Cell Bio *11*, 366–378.

1078 Novak, R., Ingram, M., Marquez, S., Das, D., Delahanty, A., Herland, A., Maoz, B.M., Jeanty,
1079 S.S.F., Somayaji, M.R., Burt, M., et al. (2020). Robotic fluidic coupling and interrogation of
1080 multiple vascularized organ chips. Nat Biomed Eng *4*, 407–420.

1081 Oliveira, S. de, Rosowski, E.E., and Huttenlocher, A. (2016). Neutrophil migration in infection
1082 and wound repair: going forward in reverse. Nat Rev Immunol *16*, 378–391.

1083 Papayannopoulos, V., Metzler, K.D., Hakkim, A., and Zychlinsky, A. (2010). Neutrophil
1084 elastase and myeloperoxidase regulate the formation of neutrophil extracellular traps. J Cell
1085 Biology *191*, 677–691.

1086 Parekh, A., Cigan, A.D., Wognum, S., Heise, R.L., Chancellor, M.B., and Sacks, M.S. (2010).
1087 Ex vivo deformations of the urinary bladder wall during whole bladder filling: Contributions of
1088 extracellular matrix and smooth muscle. J Biomech *43*, 1708–1716.

1089 Pascalis, R.D., Parnell, W.J., Abrahams, I.D., Shearer, T., Daly, D.M., and Grundy, D. (2018).
1090 The inflation of viscoelastic balloons and hollow viscera. Proc Royal Soc *474*, 20180102.

1091 Putrinš, M., Kogermann, K., Lukk, E., Lippus, M., Varik, V., and Tenson, T. (2015). Phenotypic
1092 Heterogeneity Enables Uropathogenic Escherichia coli To Evade Killing by Antibiotics and
1093 Serum Complement. Infect Immun *83*, 1056–1067.

1094 Reátegui, E., Jalali, F., Khankhel, A.H., Wong, E., Cho, H., Lee, J., Serhan, C.N., Dalli, J.,
1095 Elliott, H., and Irimia, D. (2017). Microscale arrays for the profiling of start and stop signals
1096 coordinating human-neutrophil swarming. Nat Biomed Eng *1*, 0094.

1097 Ronaldson-Bouchard, K., and Vunjak-Novakovic, G. (2018). Organs-on-a-Chip: A Fast Track
1098 for Engineered Human Tissues in Drug Development. Cell Stem Cell *22*, 310–324.

1099 Rossi, G., Manfrin, A., and Lutolf, M.P. (2018). Progress and potential in organoid research. Nat
1100 Rev Genet *19*, 671–687.

1101 Sato, T., Vries, R.G., Snippert, H.J., Wetering, M. van de, Barker, N., Stange, D.E., Es, J.H. van,
1102 Abo, A., Kujala, P., Peters, P.J., et al. (2009). Single Lgr5 stem cells build crypt-villus structures
1103 in vitro without a mesenchymal niche. Nature *459*, 262–265.

1104 Schwartz, D.J., Chen, S.L., Hultgren, S.J., and Seed, P.C. (2011). Population Dynamics and
1105 Niche Distribution of Uropathogenic Escherichia coli during Acute and Chronic Urinary Tract
1106 Infection. Infect Immun *79*, 4250–4259.

1107 Scott, V.C.S., Haake, D.A., Churchill, B.M., Justice, S.S., and Kim, J.-H. (2015). Intracellular
1108 Bacterial Communities: A Potential Etiology for Chronic Lower Urinary Tract Symptoms.
1109 Urology *86*, 425–431.

1110 Shah, P., Fritz, J.V., Glaab, E., Desai, M.S., Greenhalgh, K., Frachet, A., Niegowska, M., Estes,
1111 M., Jäger, C., Seguin-Devaux, C., et al. (2016). A microfluidics-based in vitro model of the
1112 gastrointestinal human–microbe interface. Nat Commun *7*, 11535.

1113 Si, L., Bai, H., Rodas, M., Cao, W., Oh, C.Y., Jiang, A., Nurani, A., Zhu, D.Y., Goyal, G.,
1114 Gilpin, S.E., et al. (2020). Human organs-on-chips as tools for repurposing approved drugs as
1115 potential influenza and COVID19 therapeutics in viral pandemics. Biorxiv 2020.04.13.039917.

1116 Smith, Y.C., Grande, K.K., Rasmussen, S.B., and O'Brien, A.D. (2006). Novel Three-
1117 Dimensional Organoid Model for Evaluation of the Interaction of Uropathogenic Escherichia
1118 coli with Terminally Differentiated Human Urothelial Cells. Infect Immun *74*, 750–757.

1119 Solis, A.G., Bielecki, P., Steach, H.R., Sharma, L., Harman, C.C.D., Yun, S., Zoete, M.R. de,
1120 Warnock, J.N., To, S.D.F., York, A.G., et al. (2019). Mechanosensation of cyclical force by
1121 PIEZO1 is essential for innate immunity. Nature *573*, 69–74.

1122 Song, J., Duncan, M.J., Li, G., Chan, C., Grady, R., Stapleton, A., and Abraham, S.N. (2007). A
1123 Novel TLR4-Mediated Signaling Pathway Leading to IL-6 Responses in Human Bladder
1124 Epithelial Cells. Plos Pathog *3*, e60.

1125 Spaulding, C.N., Klein, R.D., Ruer, S., Kau, A.L., Schreiber, H.L., Cusumano, Z.T., Dodson,
1126 K.W., Pinkner, J.S., Fremont, D.H., Janetka, J.W., et al. (2017). Selective depletion of
1127 uropathogenic E. coli from the gut by a FimH antagonist. Nature *546*, 528–532.

1128 Suzuki, K., Koyanagi-Aoi, M., Uehara, K., Hinata, N., Fujisawa, M., and Aoi, T. (2019).
1129 Directed differentiation of human induced pluripotent stem cells into mature stratified bladder
1130 urothelium. Sci Rep-Uk *9*, 10506.

1131 Thacker, V.V., Sharma, K., Dhar, N., Mancini, G.-F., Sordet-Dessimoz, J., and McKinney, J.D.
1132 (2020a). Rapid endothelial infection, endothelialitis and vascular damage characterise SARS-
1133 CoV-2 infection in a human lung-on-chip model. Biorxiv 2020.08.10.243220.

1134 Thacker, V.V., Dhar, N., Sharma, K., Barrile, R., Karalis, K., and McKinney, J.D. (2020b). A
1135 lung-on-chip model of early M. tuberculosis infection reveals an essential role for alveolar
1136 epithelial cells in controlling bacterial growth. Elife *9*, e59961.

1137 Tovaglieri, A., Sontheimer-Phelps, A., Geirnaert, A., Prantil-Baun, R., Camacho, D.M., Chou,
1138 D.B., Jalili-Firoozinezhad, S., Wouters, T. de, Kasendra, M., Super, M., et al. (2019). Species-
1139 specific enhancement of enterohemorrhagic E. coli pathogenesis mediated by microbiome
1140 metabolites. Microbiome *7*, 43.

1141 Truschel, S.T., Wang, E., Ruiz, W.G., Leung, S.-M., Rojas, R., Lavelle, J., Zeidel, M., Stoffer,
1142 D., and Apodaca, G. (2002). Stretch-regulated Exocytosis/Endocytosis in Bladder Umbrella
1143 Cells. Mol Biol Cell *13*, 830–846.

1144 Wang, E.C.Y., Lee, J.-M., Ruiz, W.G., Balestreire, E.M., Bodungen, M. von, Barrick, S.,
1145 Cockayne, D.A., Birder, L.A., and Apodaca, G. (2005). ATP and purinergic receptor–dependent
1146 membrane traffic in bladder umbrella cells. J Clin Invest *115*, 2412–2422.

1147 Wang, J., Wang, C., Xu, N., Liu, Z.-F., Pang, D.-W., and Zhang, Z.-L. (2019). A virus-induced
1148 kidney disease model based on organ-on-a-chip: Pathogenesis exploration of virus-related renal
1149 dysfunctions. Biomaterials *219*, 119367.

1150 Yang, E., Chee, J.L.Y., Duraiswamy, S., Chen, S., Lees, K., and Chen, S.L. (2019). Isolation of
1151 Single Intracellular Bacterial Communities Generated from a Murine Model of Urinary Tract
1152 Infection for Downstream Single-cell Analysis. J Vis Exp Jove.

1153 Yu, Y., Kwon, K., Tsitrin, T., Bekele, S., Sikorski, P., Nelson, K.E., and Pieper, R. (2017).
1154 Characterization of Early-Phase Neutrophil Extracellular Traps in Urinary Tract Infections. Plos
1155 Pathog *13*, e1006151.

1156 Zahler, S., Kowalski, C., Brosig, A., Kupatt, C., Becker, B.F., and Gerlach, E. (1997). The
1157 function of neutrophils isolated by a magnetic antibody cell separation technique is not altered in
1158 comparison to a density gradient centrifugation method. J Immunol Methods *200*, 173–179.

1159 Zalewska-Piątek, B., Olszewski, M., Lipniacki, T., Błoński, S., Wieczór, M., Bruździak, P.,
1160 Skwarska, A., Nowicki, B., Nowicki, S., and Piątek, R. (2020). A shear stress micromodel of
1161 urinary tract infection by the Escherichia coli producing Dr adhesin. Plos Pathog *16*, e1008247.

1162 Zhou, M., Zhang, X., Wen, X., Wu, T., Wang, W., Yang, M., Wang, J., Fang, M., Lin, B., and
1163 Lin, H. (2016). Development of a Functional Glomerulus at the Organ Level on a Chip to Mimic
1164 Hypertensive Nephropathy. Sci Rep-Uk *6*, 31771.

1165
1166